

Velocity Gradients of the African Large Low Velocity Province Boundary Inferred from Backazimuth-Slowness Observations of Multipathing

Jamie Ward¹, Andy Nowacki¹, and Sebastian Rost¹

¹University of Leeds

November 22, 2022

Abstract

Large Low Velocity Provinces (LLVPs) are hypothesised to be purely thermal features or possess some chemical heterogeneity, but exactly which remains ambiguous. Regional seismology studies typically use travel time residuals and multipathing identification in the waveforms to infer properties of LLVPs. These studies have not fully analysed all available information such as measuring the direction and inclination of the arrivals. These measurements would provide more constraints of LLVP properties such as the boundary velocity gradient and help determine their nature. Here, we use array seismology to measure backazimuth (direction) and horizontal slowness (inclination) of arriving waves to identify structures causing multipathing and wavefield perturbation. Following this, we use full-wavefield forward modelling to estimate the gradients required to produce the observed multipathing. We use SKS and SKKS data from 83 events sampling the African LLVP, which has been extensively studied providing a good comparison to our observations. We find evidence for structures at heights of up to 600 km above the core-mantle boundary causing multipathing and wavefield perturbation. Forward modelling shows gradients of up to 0.7% δV s per 100 km (0.0005 km /s km) are required to produce multipathing with similar backazimuth and horizontal slowness to our observations. This is an order of magnitude lower than the previous strongest estimates of -3% δV per 50 km (0.0044 km /s km). As this is lower than found for both thermal and thermochemical structures, gradients capable of producing multipathing is not necessarily evidence for a thermochemical nature.

Velocity Gradients of the African Large Low Velocity Province Boundary Inferred from Backazimuth-Slowness Observations of Multipathing

Jamie Ward¹, Andy Nowacki¹, Sebastian Rost¹

¹School of Earth and Environment, University of Leeds

Key Points:

- Multipathing is observed using backazimuth and horizontal slowness measurements of SKS and SKKS data recorded in southern Africa.
 - Lateral velocity gradients of up to 0.7% δV_s per 100 km ($0.00050 \text{ km s}^{-1} \text{ km}^{-1}$) are required to produce the observed multipathing.
 - Lateral velocity gradients capable of producing multipathing cannot distinguish between thermal and thermochemical LLVP models.

Corresponding author: Jamie Ward, eejwa@leeds.ac.uk

Abstract

Large Low Velocity Provinces (LLVPs) are hypothesised to be purely thermal features or possess some chemical heterogeneity, but exactly which remains ambiguous. Regional seismology studies typically use travel time residuals and multipathing identification in the waveforms to infer properties of LLVPs. These studies have not fully analysed all available information such as measuring the direction and inclination of the arrivals. These measurements would provide more constraints of LLVP properties such as the boundary velocity gradient and help determine their nature. Here, we use array seismology to measure backazimuth (direction) and horizontal slowness (inclination) of arriving waves to identify structures causing multipathing and wavefield perturbation. Following this, we use full-wavefield forward modelling to estimate the gradients required to produce the observed multipathing. We use SKS and SKKS data from 83 events sampling the African LLVP, which has been extensively studied providing a good comparison to our observations. We find evidence for structures at heights of up to 600 km above the core-mantle boundary causing multipathing and wavefield perturbation. Forward modelling shows gradients of up to 0.7 % δV_s per 100 km ($0.0005 \text{ km s}^{-1} \text{ km}^{-1}$) are required to produce multipathing with similar backazimuth and horizontal slowness to our observations. This is an order of magnitude lower than the previous strongest estimates of $-3 \% \delta V_s$ per 50 km ($0.0044 \text{ km s}^{-1} \text{ km}^{-1}$). As this is lower than found for both thermal and thermochemical structures, gradients capable of producing multipathing is not necessarily evidence for a thermochemical nature.

Plain Language Summary

Of the structures observed within the Earth, ‘Large Low-Velocity Provinces’ (LLVPs) have remained enigmatic in terms of their composition and origin. LLVPs have been hypothesised to affect the Earth from surface uplift to influencing the magnetic field. Determining what LLVPs are remains a major question for those studying Earth structure.

Previous seismology studies analysing LLVPs used the time taken for the wave to travel from the earthquake to the recording station and what the seismic signals look like when they arrive. However, properties such as the direction and speed at which the waves arrive are not analysed in detail. The speed and direction of the waves can inform us about how LLVPs have perturbed the waves by phenomena such as refraction.

This study measures the direction and speed of the arriving waves that have sampled the LLVP beneath Africa. Analysing this information has lead to several structures to be identified. From modelling the full wavefield with different LLVP models, we estimate the distance over which the transition from the mantle to the LLVP happens. To replicate our observed changes in direction and speed of the waves, the transition could be 10% larger than previous estimates.

50 1 Introduction

51 Large Low Velocity Provinces (LLVPs) are roughly antipodal, low-velocity features
 52 of the lower mantle located beneath Africa and the Pacific and are surrounded by high
 53 velocity material hypothesised to be slab remnants (Bijwaard et al., 1998; Grand et al.,
 54 1997; Grand, 2002), shown in Figure 1. Since first observed, LLVPs have remained enig-
 55 matic features of the lower mantle with their origin, composition and therefore their in-
 56 fluence remaining uncertain.

57 The location of the LLVPs relative to other structures and phenomena such as sur-
 58 face uplift (Hager et al., 1985; Lithgow-Bertelloni & Silver, 1998; Bull et al., 2010), pos-
 59 sible subducted slab remnants (Hager, 1984), mantle plumes (Thorne et al., 2004; Davies,
 60 Goes, & Sambridge, 2015), large igneous provinces (Torsvik et al., 2010), Ultra Low Ve-
 61 locity Zones (McNamara et al., 2010) and outer core stratification (Mound et al., 2019)
 62 suggests LLVPs are influential on whole Earth dynamics. Despite being very significant
 63 for our understanding of global dynamics, many properties of the LLVPs are still unknown
 64 and there are several hypotheses of their origin. These hypotheses can be approximately
 65 split into those where LLVPs are purely thermal features and those in which they are
 66 chemically distinct relative to the surrounding mantle (Garnero et al., 2016). For a purely
 67 thermal feature, a common hypothesis is that LLVPs are a cluster of plumes (Schubert
 68 et al., 2004) which appear as one large slow feature because of the inherent resolution
 69 limitations from seismic tomography (Bull et al., 2009; Ritsema et al., 2007; Davies et
 70 al., 2012; Davies, Goes, & Lau, 2015). The thermochemical origin hypothesis requires
 71 a source of material chemically unique to the current lower mantle either from the pri-
 72 mordial Earth or material that has accumulated over geological time. Material from the
 73 primordial Earth is hypothesised to start as a basal layer of material that is swept into
 74 piles forming the LLVPs. Mechanisms for the origin of this base layer include a basal magma
 75 ocean (Labrosse et al., 2007), accumulation of dense melts (Lee et al., 2010) or an an-
 76 cient, iron enriched crust which was then subducted and is stable at CMB conditions (Tolstikhin
 77 & Hofmann, 2005). This basal layer could then have been swept into piles observed as
 78 LLVPs which has been shown numerically (Tackley, 1998) and experimentally (Davaille,
 79 1999). Alternatively, they could have accumulated over geological time as subducted litho-
 80 sphere in the lower mantle (Hirose et al., 1999, 2005; Christensen & Hofmann, 1994) which
 81 is swept into piles, forming the LLVPs (Mulyukova et al., 2015; Tackley, 2011). However,
 82 there is some question of the feasibility of producing negative velocity perturbations (Deschamps
 83 et al., 2012) and for the slab material to accumulate at the same rate as it is stirred into
 84 the mantle (Li & McNamara, 2013).

85 Depending on the origin of the LLVPs, our understanding of how the Earth evolved
 86 from its primordial state changes. If LLVPs are a short-lived cluster of mantle plumes,
 87 they do not need to exist in early Earth history. If they are long-lived piles of primor-
 88 dial Earth remnants, their formation and survival would need to be accounted for. Con-
 89 straining the origin of LLVPs therefore has implications for our understanding of the Earth's
 90 history as well as whole Earth dynamics.

91 To reduce the number of hypotheses, there has been a focus on determining whether
 92 LLVPs are purely thermal or thermochemical features. Their relative density could pro-
 93 vide constraints but conflicting observations have suggested both higher and lower rel-
 94 ative density (Koelemeijer et al., 2017; Ishii & Tromp, 1999; Lau et al., 2017). Anticor-
 95 relation of S-wave velocity and bulk sound speed (Masters et al., 2000; Su & Dziewon-
 96 ski, 1997) is commonly used as evidence for compositional heterogeneity for LLVPs, but
 97 this has also been interpreted as the presence of post-perovskite (Davies et al., 2012; Koele-
 98 meijer et al., 2015). The presence of strong lateral velocity gradients has been attributed
 99 to a thermochemical origin (Ni et al., 2002; To et al., 2005), but these gradients can also
 100 be replicated with purely thermal structures (Davies et al., 2012; Schuberth et al., 2009).

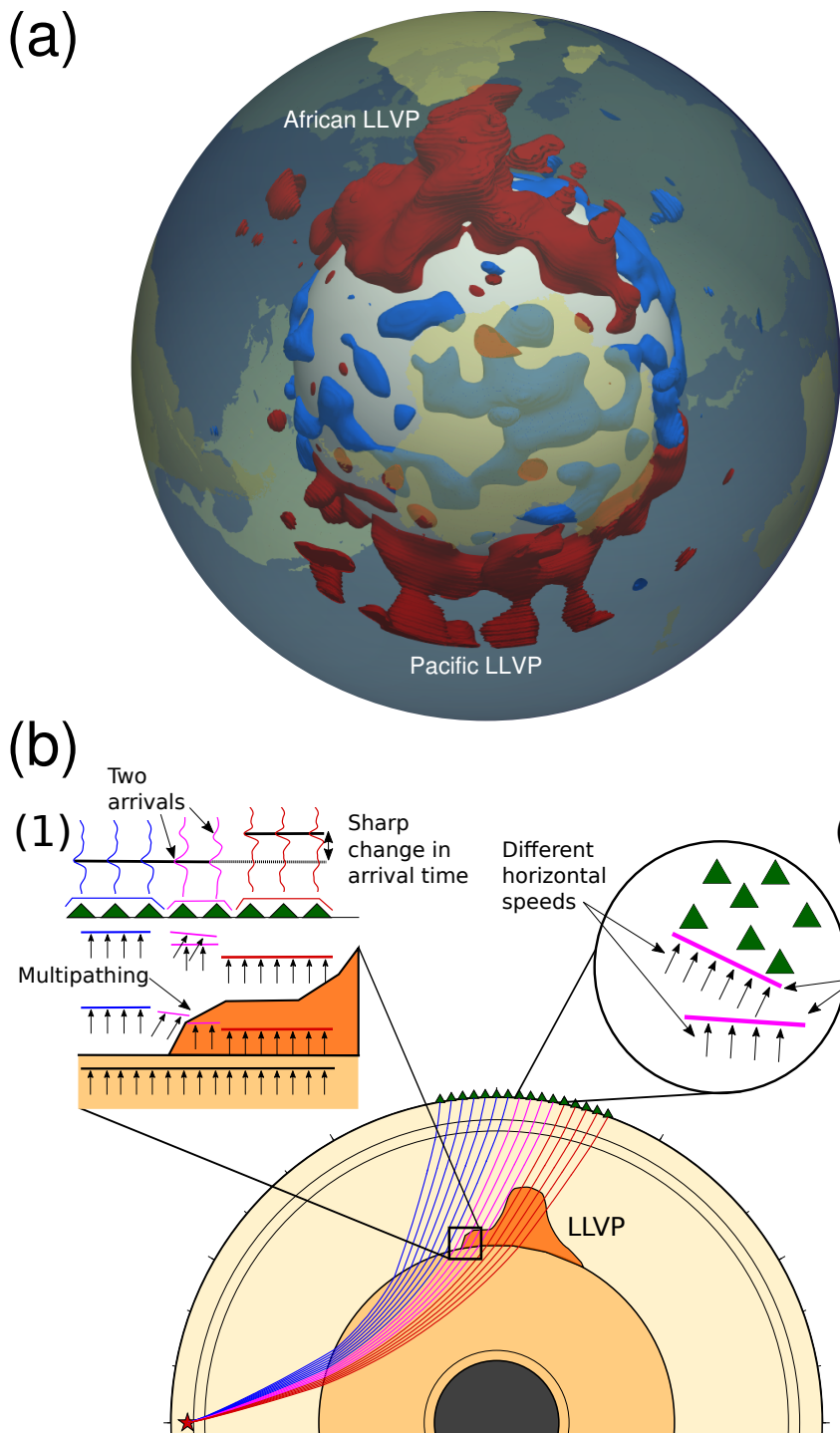


Figure 1. (a) 3D map of tomography model SEMUCB-WM1 (French & Romanowicz, 2014) with an isosurface of $-1\% \delta V_s$ shown in red and an isosurface of $+1\% \delta V_s$ in blue. The isosurface is plotted below 80% of the Earth's radius (5097 km, 2205 km above the CMB). (b) Multipathing at LLVP boundaries. As the wavefront moves over a strong lateral velocity gradient, different parts travel at different speeds and arrive at the stations at different times as two distinct arrivals (1). The gradients can cause the wave to diffract and the structure can cause the wave to refract as it passes through it. As a result, multipathed arrivals can arrive from different directions and inclinations (2).

101 Most of these studies use observations or constraints from seismological studies. Seis-
 102 mic tomography provides global, broad observations of LLVP location, morphology and
 103 relative velocity (e.g. French & Romanowicz, 2014; Ritsema et al., 2011; Simmons et al.,
 104 2010; Grand, 2002; Grand et al., 1997; Koelemeijer et al., 2015). The agreement of the
 105 long wavelength structure of LLVPs in tomography models shows they are a result of
 106 lower-mantle structure and not the different datasets or methodologies used (Lekic et
 107 al., 2012). In addition to these global observations, regional seismology studies combine
 108 travel time residuals, multipathing observations in the waveform and forward modelling
 109 to recover the location, gradient and inclination of LLVP boundaries (e.g. Ni et al., 2002;
 110 Ritsema et al., 1998; Sun & Miller, 2013; He & Wen, 2009; He et al., 2006; He & Wen,
 111 2012; To et al., 2005; Frost & Rost, 2014; Roy et al., 2019). Multipathing occurs when
 112 a wavefront is incident on a strong lateral velocity gradient that causes the wavefront
 113 to move at different speeds and arrive at a recording station with different travel times
 114 as two arrivals. In addition to this, the boundary structure causes the wave to diffract
 115 and the structure causes the waves to refract as they pass through it, so the multipathed
 116 arrivals arrive from different directions and inclinations as well as arrival times. Figure
 117 1 illustrates the multipathing phenomena at LLVP boundaries and how they can be ob-
 118 served at the surface.

119 LLVP boundary studies using travel time residuals and waveforms are common and,
 120 from their observations, have estimated the gradients at the boundaries of LLVPs to range
 121 from 3 % δV_s per 50 km ($0.0044 \text{ km s}^{-1} \text{ km}^{-1}$) (Ni et al., 2002) to 2 % δV_s per 300
 122 km ($0.00048 \text{ km s}^{-1} \text{ km}^{-1}$) (Ritsema et al., 1998) (See Table 1 for published estimates
 123 of African LLVP S-wave velocity gradients). Combining travel time residuals, multipathing
 124 identification and forward modelling to observe and infer the properties of structures is
 125 well established and has been applied to a variety of structures (Silver & Chan, 1986;
 126 Sun et al., 2019, 2010, 2017) and algorithms developed to identify multipathing auto-
 127 matically in the waveforms (Sun et al., 2009; Zhao et al., 2015). Although regional seis-
 128 mology studies only use the waveform to infer the effects of deep Earth structure on the
 129 wavefield, they do not analyse all information available such as the direction and incli-
 130 nation of the arrival.

Study	Gradient (δV_s)	Gradient ($\text{km s}^{-1} \text{ km}^{-1}$)
Ni et al. (2002)	-3% per 50 km	0.0044
Ni and Helmberger (2003c)	-3% per 100–150 km	0.0022 – 0.0015
Ni and Helmberger (2003a)	-3% per 50 km	0.0044
Sun and Miller (2013)	-3.5% per 200 km	0.0013
Ritsema et al. (1998)	-2% per 300 km	0.00048
This study	-0.7% per 100 km	0.00050

Table 1. Table of lateral gradients of the African LLVP's boundaries in δV_s and $\text{km s}^{-1} \text{ km}^{-1}$. The gradients for $\text{km s}^{-1} \text{ km}^{-1}$ were calculated using the V_s value for PREM (Dziewonski & Anderson, 1981) at the CMB

131

132 Current observations have not been sufficient to constrain LLVP properties and there-
 133 fore their composition, origin and influence remain ambiguous. Both purely thermal and
 134 thermochemical structures can replicate properties such as the strong gradients, veloc-

135 ity reduction, morphology and anticorrelation between S-wave velocity and bulk sound
136 speed (Davies et al., 2012; Schubert et al., 2009; Tackley, 1998; McNamara & Zhong,
137 2004, 2005; McNamara et al., 2010). Because current seismic observations are not enough
138 to constrain LLVP properties, new observations need to be made.

139 This study uses array seismology to measure the backazimuth (direction) and hor-
140 izontal slowness (a proxy for inclination) to identify multipathing and regions of diffrac-
141 tion and refraction in the lower mantle beneath Africa, where several studies have iden-
142 tified multipathing and sharp travel time residuals (e.g. Ni et al., 2002; Sun et al., 2009;
143 Wen et al., 2001). Different frequency bands are used to infer differences in the African
144 LLVP boundary structure such as gradient, depth and inclination. Using these obser-
145 vations, we estimate the gradients required to produce multipathing with similar back-
146 azimuth and horizontal slowness deviations as our observations and compare our esti-
147 mates to those from previous studies.

148 **2 Methodology**149 **2.1 Slowness vector grid search and beamforming**

150 To measure the backazimuth and horizontal slowness, we search over a range of slow-
 151 ness vectors each with its own backazimuth and horizontal slowness and use beamform-
 152 ing (Rost & Thomas, 2002) to measure the power of the coherent signal. If there are mul-
 153 tiple arrivals, we detect multiple arrivals with different backazimuth and horizontal slow-
 154 ness. The results are referred to as $\theta-p$ plots as they describe how the power of coher-
 155 ent signal varies with backazimuth (θ) and horizontal slowness (p). Figure 2 shows ex-
 156 amples of clear, possible and null multipathing observations. The analysis is conducted
 157 within a time window selected from visual inspection of record section, typically on the
 158 order of tens of seconds. Information such as the time windows, stations, measurements,
 multipathing identification are in the supplementary material.

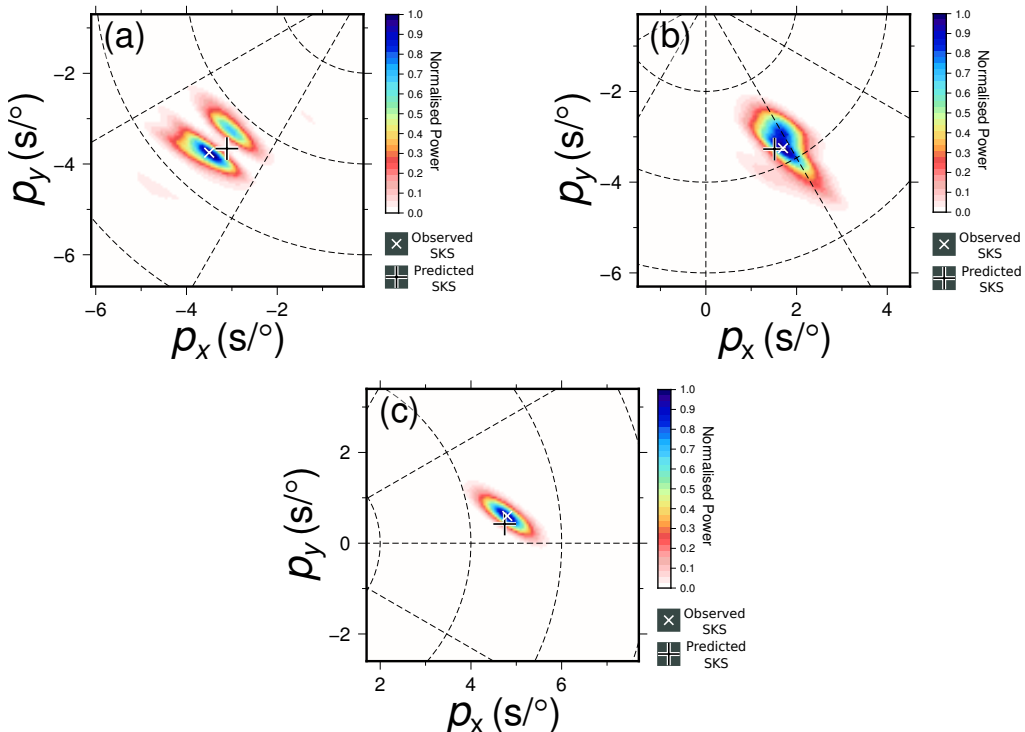


Figure 2. $\theta-p$ plots giving examples of arrivals classified as (a) clear multipathing using data from an event on 29 May, 1997, (b) potential multipathing using data from an event on 25 May, 1997 and (c) no multipathing using data from an event on 06 October, 1997. Details of event location and date are provided in the supplementary material. All of these were filtered between 0.10 and 0.40 Hz and the power linearly normalised.

159

160 Most array techniques assume energy propagates as a plane wavefront (Rost & Thomas,
 161 2002). If the array aperture is small, this assumption holds and the effect of a curved
 162 wavefront is negligible. We use data from the Kaapvaal array (James et al., 2001), which
 163 has a large aperture (spread over approximately 20° in northwest-southeast orientation)
 164 so the plane wave assumption breaks down and can contribute to some deviation from
 165 the predicted backazimuth and horizontal slowness.

166 We alter the travel time calculation of beamforming to account for a circular wave-
 167 front given a backazimuth and horizontal slowness (Figure 3). To calculate the travel times
 168 of a circular wavefront moving over a spherical Earth from event to station locations,
 169 the radial distances are calculated using the Haversine formula. This distance is then mul-
 170 tiplied by an angular slowness value in $s/\text{°}$. From these estimates, the traces are shifted,
 171 stacked and the power of the coherent signal estimated. To search over backazimuth, the
 172 event is relocated keeping the epicentral distance between the assumed event location
 173 and the mean station location constant. From this new location, the radial distance to
 174 each station is calculated relative to the mean distance and the travel times calculated
 175 (see supplementary information).

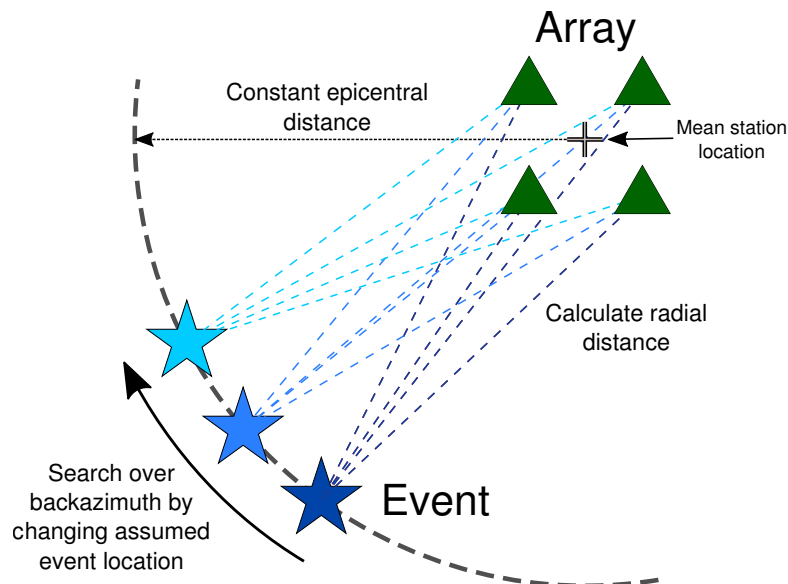


Figure 3. Illustration of the correction for a circular wavefront over a spherical Earth and how we search over backazimuth. The event location is changed depending on what backazimuth is tested with the epicentral distance kept the same. For each location, the radial distance to each station is calculated and the product of this with the angular slowness gives a travel time estimation.

176 We test our correction on synthetic data arriving from a known backazimuth and
 177 horizontal slowness (see supplementary information for further details and figures). We
 178 find our correction reduces the backazimuth deviation from 2.37° to 0.40° and the hor-
 179 izontal slowness deviation from $0.20 s/\text{°}$ to $0.03 s/\text{°}$.

180 2.2 Multipathing identification and slowness vector measurements

181 Multipathed arrivals are identified as power maxima separated in backazimuth and
 182 horizontal slowness and with a power value above the background noise and at least 10%
 183 of the maximum power value (Figure 2). The orientation is recorded for each observa-
 184 tion with clear multipathing. We calculate the orientation of the locus between the mul-
 185 tipathed arrivals relative to the vertical when multipathing is identified. This is calcu-
 186 lated from the locations of the multipathed arrivals in the $\theta - p$ observation and cal-
 187 culated the angle of the vector connecting the two points relative to the vertical. This
 188 angle is then rotated by 90° as the locus is orthogonal to the vector connecting the two
 189 points.

Our data set includes SKKS phases (Section 2.4) at distances where other phases such as S3KS could arrive at similar times and horizontal slownesses, which make it challenging to identify multipathing. For SKKS observations where multipathing could be present, we analyse synthetics generated using SYNGINE and the 1-D model prem_i_2s (Hutko et al., 2017; Krischer et al., 2017) as an estimate of the relative power of SKKS and S3KS. If there is any power for an S3KS arrival in the synthetic $\theta-p$ plots and there are multiple arrivals in the recorded data, the observation is labeled as “possible” multipathing. See supplementary information for more details.

In addition to identifying multipathing, several measurements can be made from each observation. The backazimuth residual ($\Delta\Theta$) between the observed ($\Theta_{observed}$) and the backazimuth predicted by the great circle path between the event and mean station location ($\Theta_{predicted}$) is given by $\Delta\Theta = \Theta_{observed} - \Theta_{predicted}$. The horizontal slowness residual (Δp) between the observed ($p_{observed}$) and the PREM (Dziewonski & Anderson, 1981) predicted horizontal slowness ($p_{predicted}$) is given by $\Delta p = p_{observed} - p_{predicted}$. The vector from the predicted location to the observation location in the $\theta-p$ plot is recorded as a measure of the direction and strength of the perturbation the wave has experienced. Figure 4 illustrates the meaning of this vector residual, locus between the arrivals and visualises backazimuth and horizontal slowness deviations.

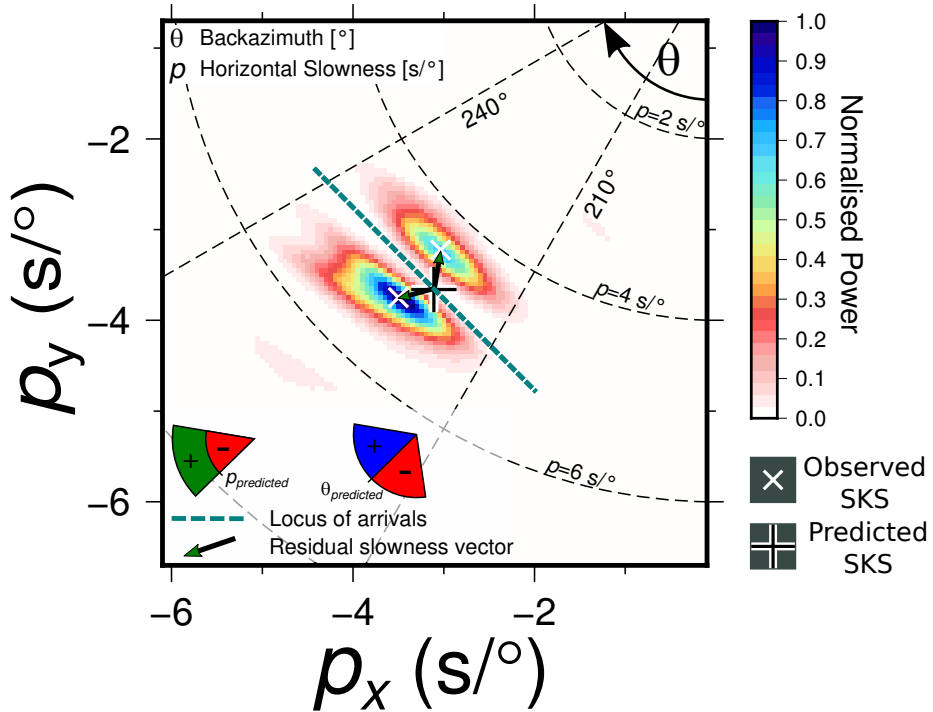


Figure 4. Annotations of the $\theta-p$ observation with data from an event on the 29 May, 1997 showing clear multipathing. The locus between the multipathed arrivals marked in blue gives an approximation of the boundary orientation. The residual slowness vector from the predicted backazimuth and horizontal slowness gives information of how the wavefield has been perturbed. Illustrations of positive and negative residuals for backazimuth and horizontal slowness are shown.

208 **2.3 Frequency Analysis**

209 To analyse the frequency dependence of multipathing and its wavefield effects, the
 210 data are filtered in five frequency bands and analysed separately (frequency bands: 0.07-
 211 0.28 Hz, 0.10-0.40 Hz, 0.13-0.52 Hz, 0.15-0.60 Hz, 0.18-0.72 Hz, 0.20-0.80 Hz) each with
 212 a width of two octaves. The frequencies will affect the size of the Fresnel zone, which gives
 213 an approximation of the area contributing to the observation. For both the main and
 214 multipathed arrival to have enough power to be observed, there needs to be a significant
 215 enough velocity change over the Fresnel zone. The frequency variation of multipathing
 216 could be indicative of differences in sharpness, depth or inclination between boundaries.
 217 Fresnel zones for each frequency band were calculated at the CMB using velocity value
 218 from PREM (Dziewonski & Anderson, 1981) and shown in the supplementary informa-
 219 tion.

220 **2.4 Data and preprocessing**

221 SKS and SKKS data (Figure 5) from events located 70° to 140° away from the cen-
 222 tre of the array and with magnitudes between 5.5 and 7.5 recorded at the Kaapvaal ar-
 223 ray are used to analyse Africa LLVP boundary structure (Figure 5). We deconvolve the
 224 instrument response, remove the mean amplitude, taper and apply a bandpass filter be-
 225 tween 0.05 and 1.0 Hz (period of 1–20 s) for visual inspection. The horizontal com-
 226 ponents are rotated to radial and tangential components for clear SKS and SKKS identi-
 227 fication. Following this, the signal-noise ratio (SNR) is estimated in a 70s time window
 228 around the predicted arrival time and used to roughly sort the data into traces that should
 229 be kept ($\text{SNR} > 3$), removed ($\text{SNR} < 2.5$) and could be used ($2.5 < \text{SNR} < 3$). Events
 230 with more than 10 traces sorted into “keep” or more than half between the “keep” and
 231 the potentially usable bins were sorted by hand after visual inspection of the record sec-
 232 tion aligned on the PREM (Dziewonski & Anderson, 1981) predicted SKS arrival. If there
 233 is a clear SKKS arrival, SKKS is also analysed. 83 events remain (see supplementary ma-
 234 terial for event details).

235 The frequency bands we use are limited by the station spacing of the array. If the
 236 inter-station spacing is too large, spatial aliasing could occur in the $\theta - p$ plot and be
 237 misidentified as multipathing. The Nyquist criterion for the station spacing of each fre-
 238 quency band is used to limit the frequencies used. The lower frequencies will likely have
 239 higher amplitudes and influence the stacking significantly more than the higher frequen-
 240 cies, so we only limit the lower frequency cut offs for the frequency analysis using this
 241 criterion. The lower frequency cut-off is limited to 0.20 Hz.

242 **2.5 Noise reduction techniques**

243 Multipathed arrivals could arrive with a lower SNR and stack to a similar power
 244 as incoherent signal at other backazimuths and horizontal slownesses. To aid multipathing
 245 identification, several techniques to improve the SNR of coherent arrivals are implemented.
 246 We use phase weighted stacking (Schimmel & Paulssen, 1997), F-statistic (Blandford,
 247 1974) and deconvolve the array response function (ARF) using the Richardson-Lucy de-
 248 convolution method (Richardson, 1972; Lucy, 1974) as done in previous studies (Picozzi
 249 et al., 2010; Maupin, 2011). These are detailed further in the supplementary informa-
 250 tion with examples of their effectiveness. We use the outputs of all these methods to iden-
 251 tify multipathing in the data with criteria for clear, potential and no multipathing ex-
 252 plained in Section 2.2. Measurements of horizontal slowness and backazimuth deviations
 253 are taken using the phase-weighted (Schimmel & Paulssen, 1997) stack points as they
 254 most consistently have lower noise than the other methods.

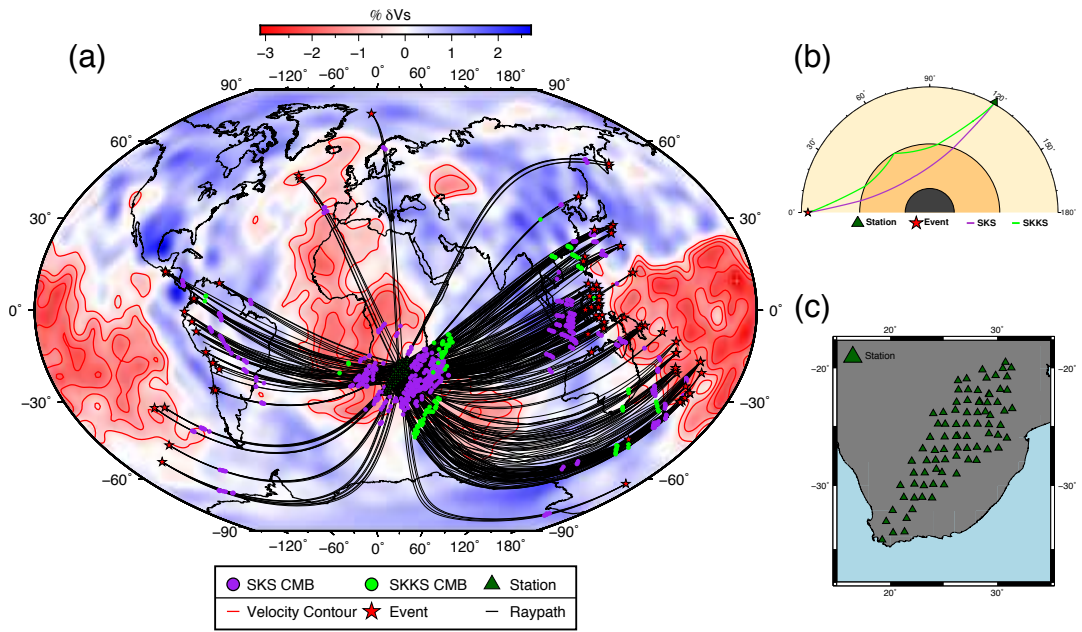


Figure 5. (a) The CMB pierce point locations for SKS and SKKS from events used in the analysis (Section 2.1) for whole array and sub array observations (Section 2.6). The earthquakes, stations and ray paths are also plotted to show what other structures could have been sampled. The paths provide good coverage of the African LLVP, its boundaries and the surrounding mantle. The pierce points are shown on tomography model S40RTS (Ritsema et al., 2011) with shear wave velocity contours of -0.5% , -1.0% , -1.5% and -2.0% δV_s marked to highlight potential boundaries and structure. (b) Paths of SKS (purple) and SKKS (green) through the Earth. (c) Station coverage of the Kaapvaal array, chosen for its excellent station density and coverage.

255

2.6 Sub arrays

256

To better constrain the location of multipathing and its wavefield effects, the available stations in the Kaapvaal array are grouped into sub arrays. Data from all available stations are also analysed. We group the traces using their waveform properties, back-azimuths and epicentral distances. We accept that we are adding our own bias to the observations by grouping the sub arrays this way. Whole array observations are used to identify multipathing but, because the large area of the combined Fresnel zones of the Kaapvaal array, not used to analyse backazimuth and horizontal slowness deviations. 317 different sub array geometries were used; stations for each sub array are given in the supplementary material.

264

265

2.7 Method strengths and limitations

266

Other studies have developed a method to automatically detect multipathing in the waveform (Sun et al., 2009). In comparison to this method, there are several limitations and advantages. The multipathed arrivals need to be present in enough traces to stack coherently and produce clear arrivals on the $\theta-p$ plot. Arrivals of similar slowness may not be resolved as separate arrivals. On the other hand, noisier traces can be used because the stacking methods improve the SNR. The observations themselves also allow measurements of backazimuth and horizontal slowness deviations, which can be used to analyse structures affecting the wavefield.

267

268

269

270

271

272

273

274 **3 Multipathing**

275 This section describes our multipathing observations and discusses the frequency
 276 dependence (Section 3.1) and spatial variation (Section 3.2) with interpretations of pos-
 277 sible boundary locations. Clear multipathing is observed in 16% of our whole array ob-
 278 servations and 6.6% of our sub array observations.

279 **3.1 Frequency dependence**

280 Figure 6 shows the spatial variability of multipathing with different frequency bands.
 281 Some observations show clear multipathing within specific frequency bands while oth-
 282 ers in all frequency bands, which could be due to differences in the nature of the bound-
 283 eries such as the velocity gradient, inclination or depth. As explained in Section 2.3, to
 284 observe multipathed arrivals, enough of the Fresnel zone needs to sample different ve-
 285 locities. This requires the lateral velocity gradient needs to be sufficiently strong, and
 sufficiently sampled by the wavefield.

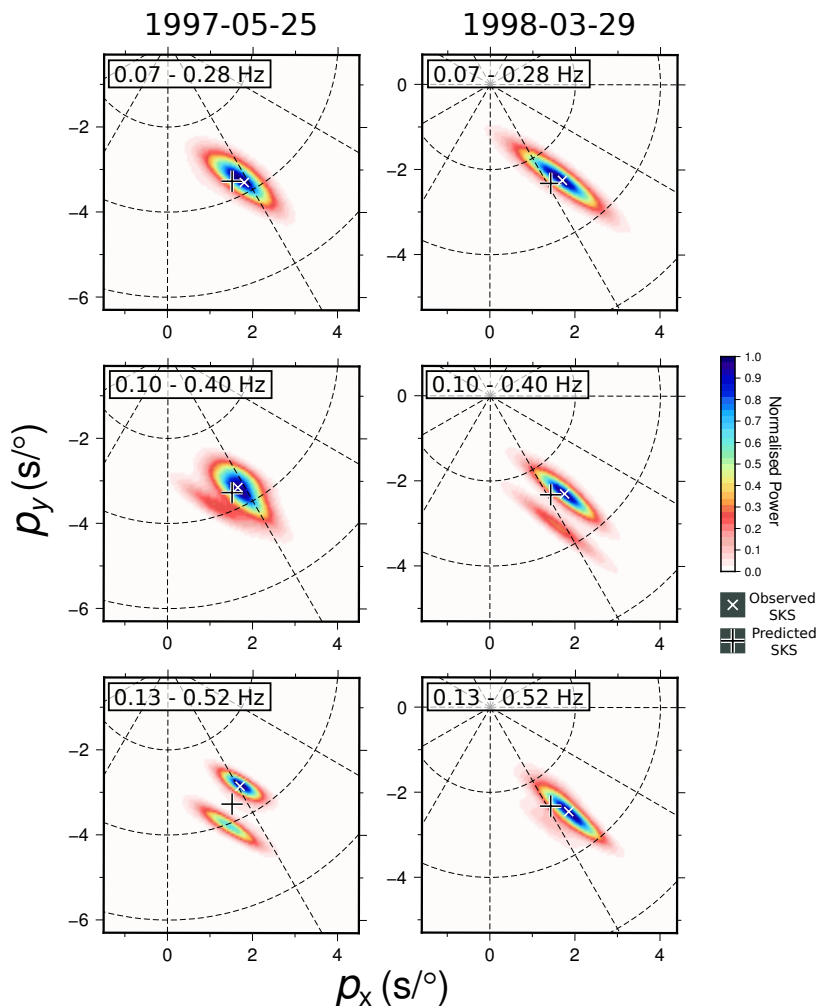


Figure 6. A comparison of the frequencies clear multipathing is observed for two different events. The left column shows θ - p plots using data from the 25 May 1997 event and clear multi-
 pathing is only observed in the 0.13 – 0.52 Hz band. The right column shows θ - p plots using data
 from the 29 March 1998 event where clear multipathing is only observed in the 0.10 – 0.40 Hz
 frequency band.

286 Observations of multipathing at high frequencies could be due to differences in wave-
 287 length or indicative of strong velocity gradients while multipathing at low frequencies
 288 indicative of a significant velocity change over a wider boundary. If the boundary is at
 289 an angle to the incidence of the wave, the boundary will not be sampled for as long and
 290 appear smoother.

291 Sampling boundaries at different depths could cause frequency variation in our ob-
 292 servations due to changes of wavelength with velocity. At the same depth, and therefore
 293 the same 1-D velocity, the boundaries need to have different gradients or inclinations for
 294 multipathing to occur at different frequencies. At different depths, the boundaries could
 295 be the same sharpness and inclination, but observed at different frequencies due to dif-
 296 ferent Fresnel zone sizes.

297 The size and station density of the array could contribute to the frequency vari-
 298 ation. Larger, denser arrays will be sensitive to a larger area and will record multipathed
 299 arrivals in more waveforms. Lower frequencies with larger Fresnel volumes are more sen-
 300 sitive to weaker velocity gradients, but the weaker gradients may mean the multipathed
 301 arrivals will have a smaller amplitude also. Whole array observations should have more
 302 multipathing observations at lower frequencies (Figure 7) because weaker multipathed
 303 arrivals will be recorded in more waveforms and stack to an observable power.

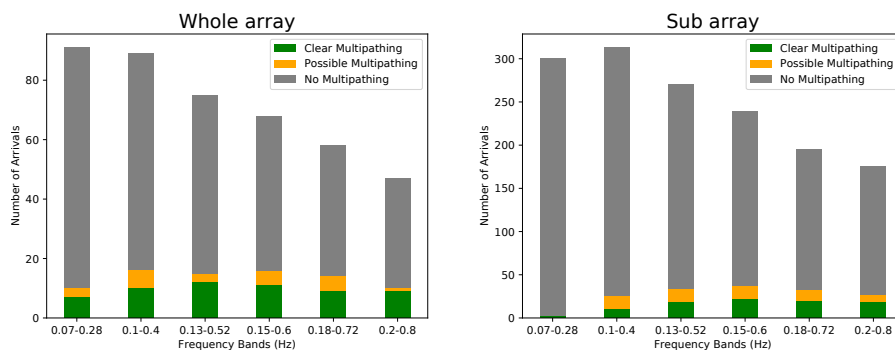


Figure 7. Number of observations of clear (green), possible (yellow) and no multipathing (grey) in different frequency bands for whole array and sub array observations. The number of usable observations changes with frequency due to noise conditions and slowness resolution. At higher frequencies the observations were noisier and at the lowest frequencies the slowness resolution is too poor to use.

304 3.2 Spatial analysis

305 Spatially analysing our observations shows multipathing is not limited to one re-
 306 gion and occurs in different frequency bands depending on the region. In Figure 8, the
 307 loci and the tomography velocity contours for both whole and sub array observa-
 308 tions align well to the east of Africa (25°S , 32°W) with a boundary trending northwest-southeast
 309 which then curves to trend approximately west-east as the boundary moves southward.
 310 In these regions, multipathing is observed in all frequency bands over both whole and
 311 sub array observations. The range of frequencies could be interpreted as an LLVP bound-
 312 ary being sampled at several depths, or a boundary with both a strong lateral velocity
 313 gradients and a significant velocity change.

314 The circular low velocity feature to the southeast of Africa (35°S , 30°W) marked
 315 by -1.5% δV_s velocity contour aligns well with the loci in the area. Multipathing is ob-
 316 served at a range of different frequencies here with arguably more observations at fre-
 317 quencies above the $0.15 - 0.60$ Hz band. Observing multipathing at higher frequencies
 318 imply sampling of a relatively sharp gradient and observations in a broad frequency range
 319 suggest large and sharp velocity changes or sampling boundaries at several depths.

320 To the west of Africa (25°S , 15°W), particularly in the sub array observations, there
 321 is a lot of scatter in loci orientations and multipathing is mainly observed in the higher
 322 frequency bands. The scattered loci are possibly due to the waves travelling through the
 323 body of the LLVP boundaries and sampling boundaries at several depths. Depending
 324 on the depth, the boundaries could have different orientations, therefore leading to scat-
 325 tered loci. Observing multipathing in higher frequency bands could be due to strong lat-
 326 eral velocity gradients or the depths the boundaries have been sampled.

327 Studies using travel time and waveform observations have reported a boundary to
 328 the southwest of Africa with an approximate northwest-southeast strike (Ni et al., 2002).
 329 The orientation of the locus of our multipathed arrival in this region approximately agrees
 330 (Figure 8) supporting these previous results. Sun et al. (2010) find evidence for a man-
 331 tle plume in the mid-mantle of this region too. We do not find evidence for this, most
 332 likely because of resolution and sampling limitations.

333 To further explore the spatial distribution of multipathing, we compare the loca-
 334 tions of clear, possible and no multipathing observed at any frequency (Figure 9). Mul-
 335 tipathing is not limited to one region and the pierce points of clear multipathing are very
 336 close to pierce points that show no or unclear multipathing. Our interpretation is the
 337 boundary structure needs to be sampled in a specific way for the multipathed arrivals
 338 to arrive with observable amplitudes.

339 3.3 Seismic anisotropy

340 There have been several studies analysing seismic anisotropy in the region of this
 341 study (e.g. Lynner & Long, 2014; Ford et al., 2015; Wang & Wen, 2007a; Reiss et al.,
 342 2019; Cottaar & Romanowicz, 2013). Shear wave splitting could complicate the wave-
 343 forms and be misinterpreted as multipathing. Therefore, we measure SKS splitting in
 344 splitting time and direction of the fast axis, remove the measured effect and repeat the
 345 analysis for a selection of events. After the anisotropy correction, we still observe mul-
 346 tipathing. For low SNR events, correcting for anisotropy reduced the quality of the ob-
 347 servation. Since anisotropy alone is not the cause of observed multipathing and can re-
 348 duce the quality of some observations, we do not correct for shear wave splitting.

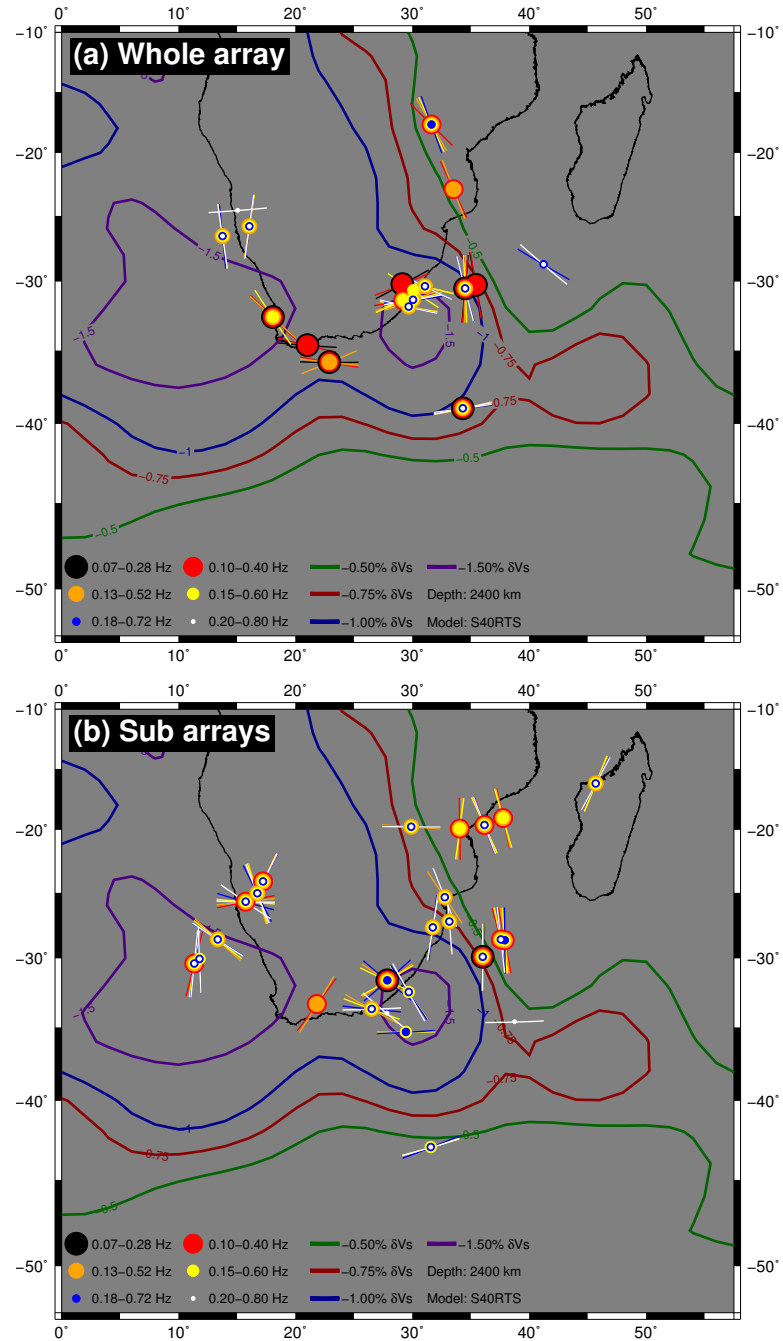


Figure 8. 1-D ray path pierce points at 2400 km depth (approximately 500 km above the CMB) for events showing clear multipathing. **(a)** whole array observations and **(b)** sub array observations. The size and colour of the circles correspond to the frequencies at which multipathing is observed. The locus between the arrivals is marked for each frequency to represent the approximate orientation of the boundary causing the multipathing. Velocity contours are shown at 2400 km depth from tomography model S40RTS (Ritsema et al., 2011).

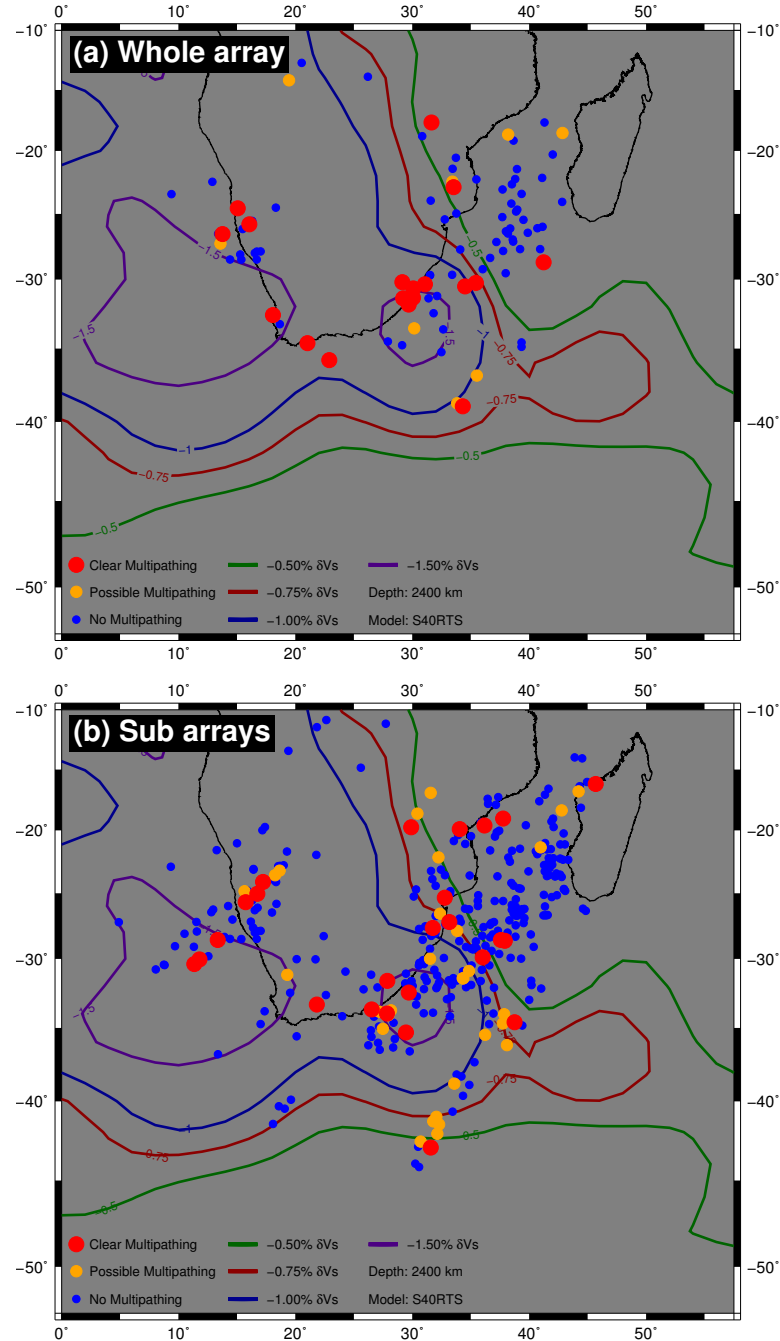


Figure 9. 1-D ray path pierce points at 2400 km depth (approximately 500 km above the CMB) with clear (red), possible (orange) and no (blue) multipathing at any frequency for (a), whole array observations and (b) sub array observations. Clear multipathing at any frequency, it is labeled as ‘clear’, potential multipathing is labeled as ‘possible’, no indication of multipathing at any frequency is labeled as ‘no’ multipathing.

349 **4 Slowness Vector Residuals**

350 We spatially analyse backazimuth, horizontal slowness and slowness vector devi-
 351 ations to identify regions of wavefield perturbations. Descriptive interpretations are given
 352 in Sections 4.1 to 4.3. When analysing these deviations, the pierce point location is moved
 353 to match observed backazimuth and horizontal slowness.

354 **4.1 Backazimuth Deviations**

355 Spatial analysis of backazimuth deviations (Figure 10) reveals several patterns in-
 356 dicative of structures perturbing the wavefield. The most distinct pattern is to the south-
 357 east of Africa (35°S , 27°W) where positive backazimuth residuals (blue, arriving from
 358 more clockwise direction than predicted) to negative backazimuth residuals (red, arriv-
 359 ing from more anticlockwise direction than predicted) then moving northeast (25°S , 40°W)
 360 to negligible backazimuth residuals (white, arriving as predicted). The transition from
 361 positive to negative residuals implies there are two boundaries being sampled causing
 362 diffraction in opposite directions. We interpret this as the circular structure southeast
 363 of Africa marked by the -1.5% δV_s velocity contours in Figure 10.

364 We detect more negative backazimuth residuals than positive (supplementary in-
 365 formation) with the negative residuals also spread over a larger area. Some of the neg-
 366 ative residuals could be caused by the same circular feature described above, but as the
 367 pierce point locations move northeast, the LLVP boundary trending in a northwest-southeast
 368 orientation could be contributing. Further north, the negative deviations sharply tran-
 369 sition to negligible residuals implying they are not sampling a structure or boundary that
 370 would cause the wavefront to change direction. Either a boundary orthogonal to wave
 371 propagation or structures causing the wave to vertically refract with no change to the
 372 horizontal propagation direction are possibilities. We discuss this further when analysing
 373 the horizontal slowness deviations in Section 4.2.

374 Analysing the distribution of the backazimuth residuals shows little variation be-
 375 tween frequency bands (supplementary information). The majority of the observations
 376 lying between approximately 8° and -14° and maximum values of 10° to -22° for pos-
 377 itive and negative deviations respectively. There are more negative residual observations
 378 with on average approximately 64% negative residual observations compared to 36% pos-
 379 itive. This is possibly because of the heterogeneous sampling from limited event-station
 380 configurations.

381 **4.2 Horizontal slowness deviations**

382 The spatial distribution of horizontal slowness residuals in Figure 11 offers a less
 383 clear picture than the backazimuth residuals. The circular feature defined by -1.5% δV_s
 384 contours to the southeast of Africa (35°S , 30°W) does show some pattern with the neg-
 385 ative residuals lying on the northwest side of the feature, closer to the array, and the pos-
 386 itive residuals on the southeast side. Negative residuals mean the wave is arriving more
 387 steeply and positive residuals more shallowly, which is expected if the circular feature
 388 diffracts the waves.

389 Observations to the east of Africa (25°S , 40°W) show a transition from positive
 390 (green) to negative (red) residuals most of which also have very small backazimuth devi-
 391 ations. If the wave has passed through material that is slower or faster than the 1-D
 392 velocity value at that depth from PREM (Dziewonski & Anderson, 1981), the wave would
 393 refract to arrive at a different inclination and horizontal slowness, but with negligible back-
 394 azimuth deviations. For the transition to be this abrupt, adjacent fast and slow struc-
 395 tures such as slab remnants near a LLVP boundary would be needed. The location of
 396 fast structures relative to the LLVP boundary at the core-mantle boundary in tomog-
 397 raphy model SEMUCB-WM1 (French & Romanowicz, 2014) aligns well with the tran-

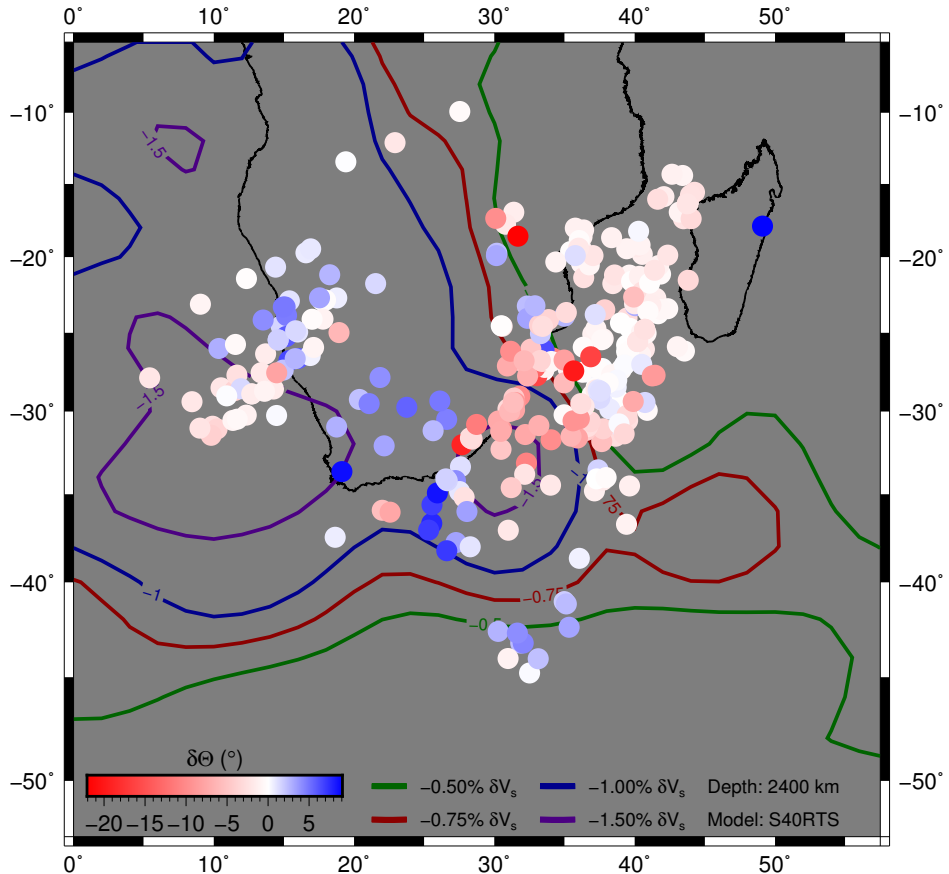


Figure 10. Pierce points for sub array observations (frequency band 0.13 Hz to 0.52 Hz) at 2400 km depth coloured by backazimuth deviations relative to the great circle path. Blue colours show paths that arrive from a more clockwise direction and red show paths arriving from a more anticlockwise direction than predicted. Contours from S40RTS (Ritsema et al., 2011) at a depth of 2400 km are shown to represent potential structures causing the observations. Pierce points are corrected to the measured horizontal slowness and backazimuth.

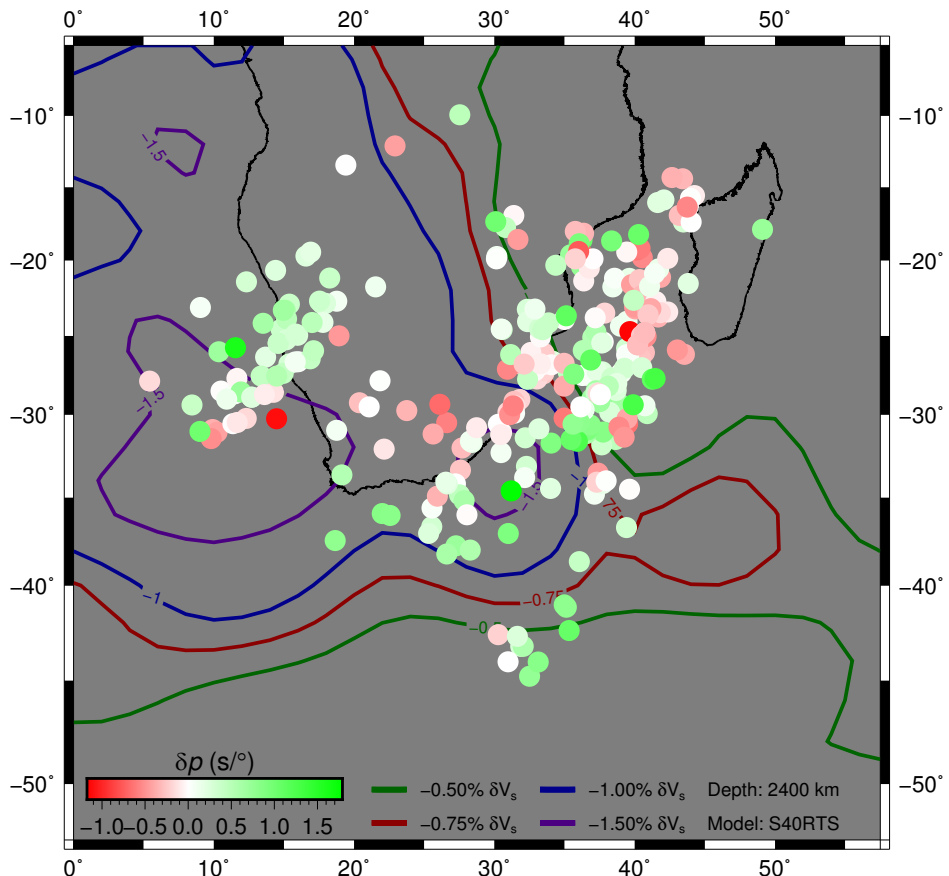


Figure 11. Pierce points for sub array observations (frequency band 0.13 Hz to 0.52 Hz) at 2400 km depth, coloured by horizontal slowness deviations relative to the PREM predicted ray parameter (Dziewonski & Anderson, 1981). Contours from S40RTS (Ritsema et al., 2011) at a depth of 2400 km are marked to outline structures potentially contributing to the observations. Pierce points are corrected to match the observed horizontal slowness and backazimuth.

398 sition (Figure 12), implying these structures could be the cause of our observations. Given
 399 the size of the sub-arrays and the size of the Fresnel zone at these frequencies, it is pos-
 400 sible this fast structure is causing the waves to refract and arrive at a steeper inclina-
 401 tion with negligible backazimuth deviation.

402 Residuals west of Africa (25°S , 15°W) are mainly positive, so arrive at a shallower
 403 angle, and travel through the body of the LLVP causing the waves to refract. However,
 404 there are also several multipathed arrivals in this region with scattered loci (Figure 8)
 405 suggesting the waves also sample a boundary but, because the loci are scattered, it is
 406 difficult to constrain exactly what is causing these observations.

407 The horizontal slowness deviations have little variation with frequency, with most
 408 observations lie between 1.2 s° and -1.0 s° (supplementary information). Outliers are
 409 present in these observations, but show no clear pattern and range from a maximum of
 410 2.1 s° and a minimum of -1.6 s° . Like the backazimuth residuals, the observations
 411 are not evenly distributed about 0 s° with 60% positive residuals and 40% negative.
 412 This variation could be due to the dominantly slow mantle structure beneath Africa caus-
 413 ing them to refract and arrive at a shallower angle.

414 4.3 Full Slowness Vector Deviations

415 The full slowness vector deviation is a vector from the predicted arrival in the $\theta-$
 416 p plot to the observed arrival. The azimuth of the vector indicates the direction of per-
 417 turbation and the length is indicative magnitude. This vector combines the backazimuth
 418 and horizontal slowness perturbations giving a clear picture of how the wavefield is be-
 419 ing affected. Figure 13 shows how these vectors vary spatially.

420 The radial pattern and magnitude of the vectors around the circular feature south-
 421 east of Africa (35°S , 30°W) support our interpretation that this structure is the cause
 422 of our observations. Northeast of this region, the azimuths change their orientation to
 423 be approximately orthogonal to the velocity contours of the boundary striking northwest-
 424 southeast. Further northeast (25°S , 40°W) the vectors have opposite azimuths shown
 425 by the colour change from red to green in the vector heads. The paths of these waves
 426 suggest they may not sample the LLVP boundary, supporting the hypothesis of fast and
 427 slow regions refracting the waves at depth. The vector residuals west of Africa (25°S ,
 428 15°W) are more scattered than in other regions but generally have an azimuth point-
 429 ing away from the array and arrive at a shallower inclination. The scattered vector resi-
 430 dials, the scattered loci and the presence of multipathing in this region suggests the wave-
 431 field is being affected by several boundaries at different depths and the body of the LLVP.

432 The magnitude of the slowness vector deviations does not vary greatly with fre-
 433 quency with slightly more high magnitude deviations at higher frequencies and with min-
 434 imum and maximum observed values from less than 0.1 s° to 2.1 s° (supplementary
 435 information).

436 Previous studies have analysed similar regions and show some evidence for struc-
 437 tures we observe. Sun et al. (2009) analyse regions of the lowermost mantle similar to
 438 areas where we find boundaries between slow and fast structures and a quasi-circular struc-
 439 ture. Using their multipath detector method with S_{diff} data from the 22 December 1997
 440 event, they identify a region with strong gradients southeast of Africa in a similar re-
 441 gion to the hypothesised boundary in Figure 12. Their travel time residuals transition
 442 from negative to positive over this region supports our interpretation of a transition from
 443 a slow to a fast structure. The results using data from the 04 September 1997 event show
 444 evidence for smaller scale structure southeast of the Kaapvaal array with a similar struc-
 445 ture and approximate location as our observed circular structure.

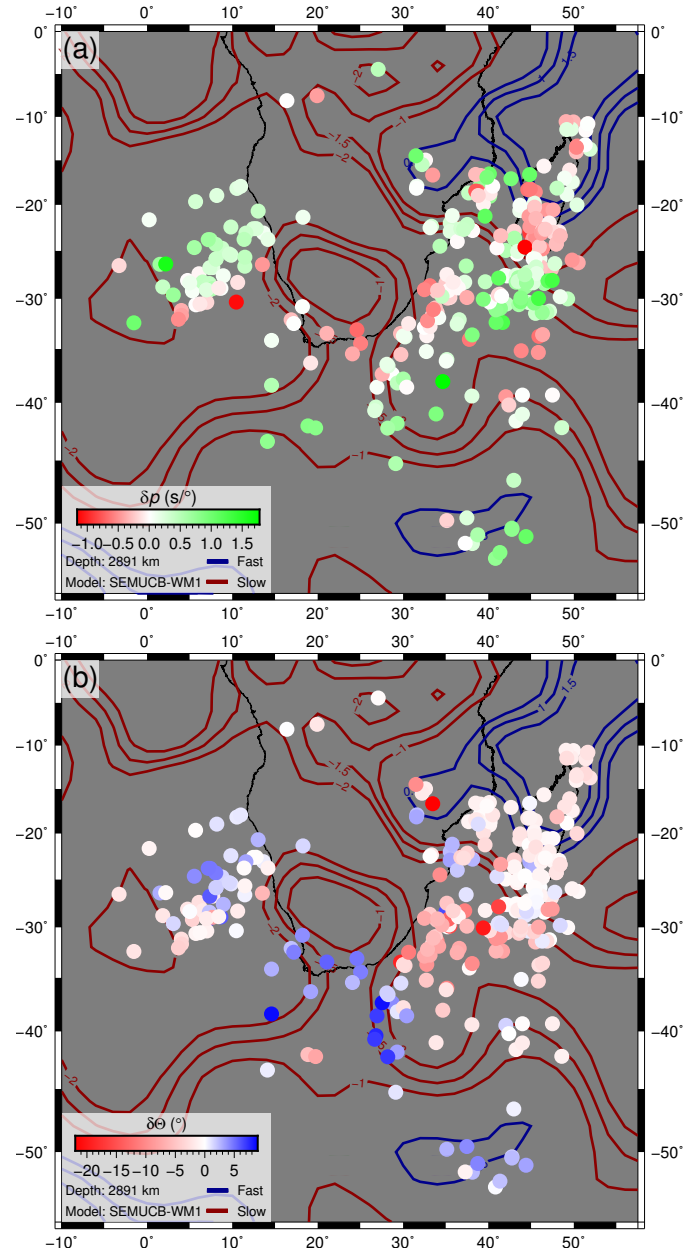


Figure 12. Pierce points at the CMB coloured with (a) horizontal slowness deviations and (b) backazimuth deviations. Negative contours -1.0% , -1.5% , -2.0% δV_s and positive contours 0.5% , 1.0% , 1.5% δV_s of tomography model SEMUCB-WM1 (French & Romanowicz, 2014) are shown to highlight the transition from fast to slow structures east of Africa. The events have been relocated so the 1-D paths arrive from the observed backazimuth and horizontal slowness.

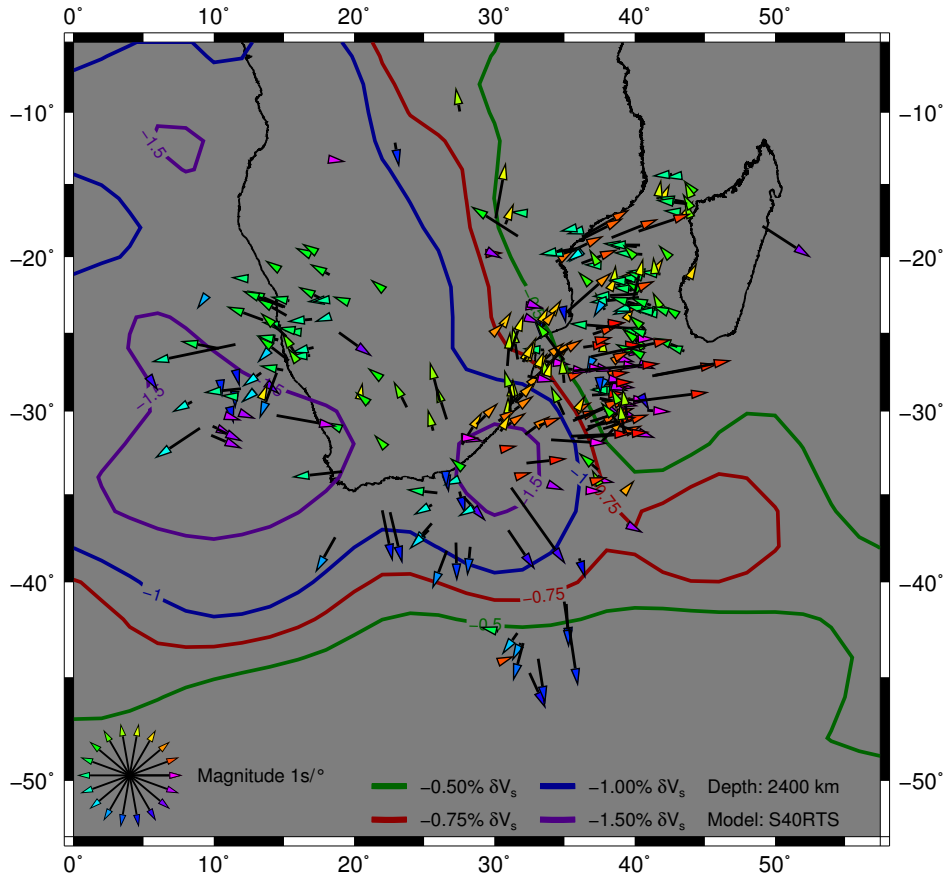


Figure 13. Pierce points for sub array observations showing the full slowness vector deviation from the prediction to the observation in the θ - p plot coloured by azimuth (Figure 4). The contours from S40RTS (Ritsema et al., 2011) and the pierce points are marked at a depth of 2400 km to outline potential structures contributing to the observations. The frequency band used is from 0.13 Hz to 0.52 Hz. The pierce points have been relocated according to the observed backazimuth and horizontal slowness.

446 5 Forward modelling and comparison to tomography models

447 This section explores the properties required to observe multipathing through forward
 448 modelling and compares our estimated velocity gradient to previous studies. The
 449 velocity gradients at the boundary of LLVPs are frequently used as evidence for chem-
 450 ical heterogeneity (e.g. Ni et al., 2002; To et al., 2005; Wen et al., 2001). These veloc-
 451 ity gradients were estimated by replicating travel time residuals and waveforms via for-
 452 ward modelling. In this section, we replicate conditions for multipathing to be observed
 453 using this method and how these conditions compare to that of other studies (Table 1).

454 We use SPECFEM3D (Komatitsch & Tromp, 2002b, 2002a), to create synthetic
 455 data for three earthquakes (Section 5.1) which show multipathing at frequencies that can
 456 be modelled. As the modelling is computationally expensive, we limit ourselves to these
 457 events and model frequencies up to approximately 0.18 Hz. We test the effects of ellip-
 458 ticity and topography and find they have a negligible effect.

459 The loss of small-scale heterogeneity and reduction of velocity amplitude and gra-
 460 dients in seismic tomography from regularisation, smoothing and limited sampling cov-
 461 erage is well documented (Ritsema et al., 2007; Foulger et al., 2013; Schuberth et al., 2009;
 462 Bull et al., 2009). Given the large parameter space of a 3-D structure that could cause
 463 multipathing, we take the structure of tomography as an approximation of long-wavelength
 464 Earth structure and accept the mentioned limitations. From this starting point, we in-
 465 crease the velocity perturbations and gradients linearly to approximately account for the
 466 reduction through tomographic filtering and recreate conditions for multipathing to be
 467 observed in our method.

468 S40RTS (Ritsema et al., 2011) is used as a starting point as the velocity contours
 469 shown in figures in Sections 3 and 4 provide possible explanations for our observations.
 470 In each model, the velocity perturbations have been amplified at depths greater than 1000
 471 km and depths shallower than 660 km are unchanged. The transition from the ampli-
 472 fied lower mantle to the upper mantle is tapered to avoid artefacts. No crustal model
 473 is used in our modelling as test show no identifiable effect of crustal structure on our ob-
 474 servations. Three models are used where perturbations at depths greater than 1000 km
 475 have been doubled (labeled as M2), trebled (M3), quadrupled (M4) and we use S40RTS
 476 (Ritsema et al., 2011) with no amplification (M1).

477 5.1 Gradients of boundaries

478 We compare observations of SKS data from events on the 25 May 1997, 28 March
 479 1998 and 28 May 1997 to runs using all models described earlier. Figure 14 shows the
 480 $\theta - p$ plots of the synthetic data with the observations.

481 For all events, the S40RTS (Ritsema et al., 2011) velocity perturbations are not
 482 sufficient to cause detectable multipathing, indicating that stronger gradients are required.
 483 In models with stronger gradients, whether multipathing is observed and how similar it
 484 is to the observation varies with the event likely due to the different sampling geome-
 485 try. Synthetic data for the 25 May 1997 in model M3 shows clear multipathing where
 486 the relative power and location of the two arrivals are similar to the observation. In model
 487 M2, there is no clear multipathing and the location of the arrival is approximately the
 488 average of the locations of the observed multipathed arrivals. As the only difference be-
 489 tween M2 and M3 is the strength of amplitudes in the lower mantle, we argue it is lower
 490 mantle structure causing the observed multipathed arrivals in this event.

491 The 29 May 1997 event shows some weak multipathing in all amplified models in
 492 similar locations to the observation, but the arrivals do not have the same relative power
 493 in the $\theta - p$ plot. This suggests there is a boundary being sampled, but the gradient in
 494 the model is weaker or the pathlength along the boundary is shorter than in the data.

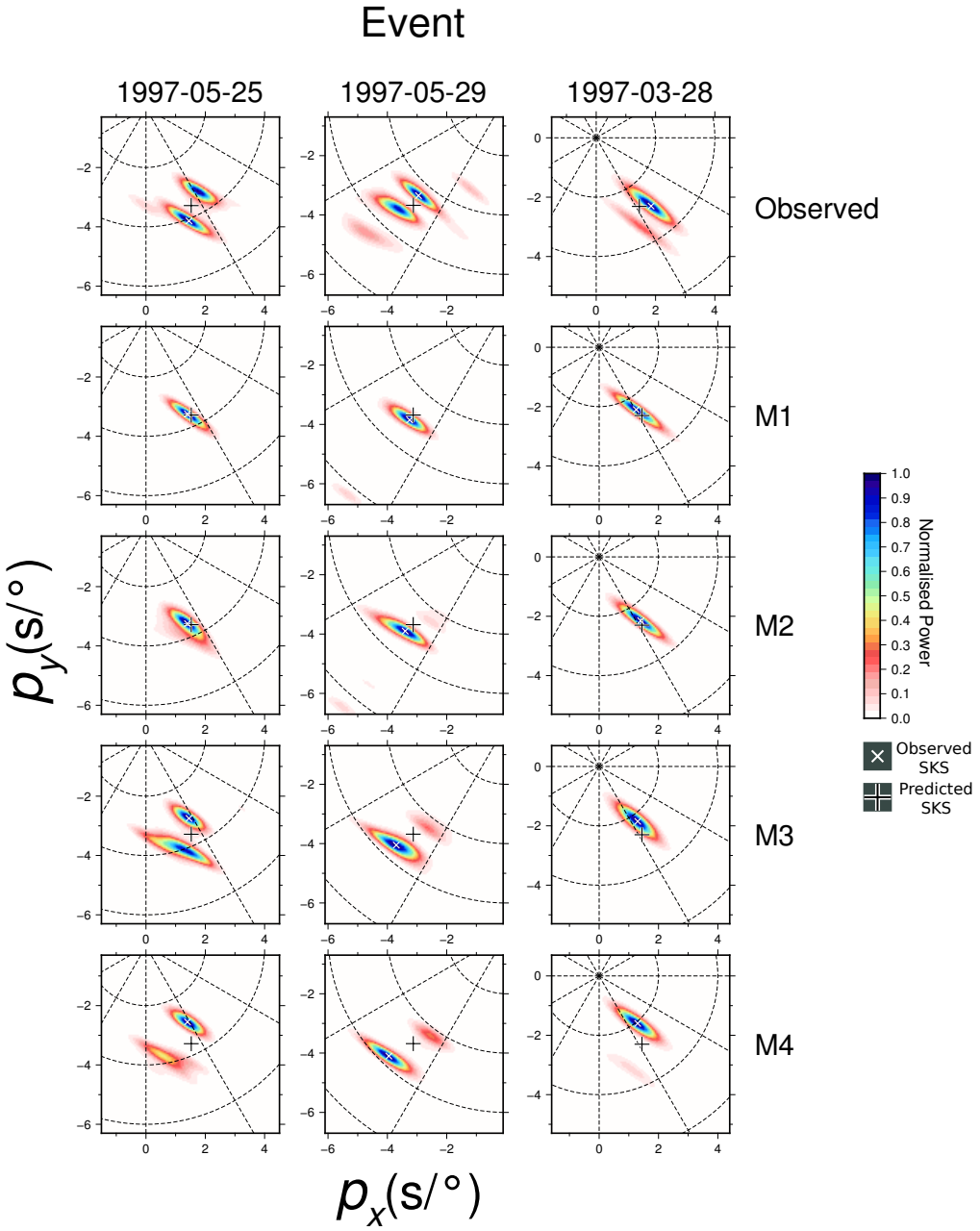


Figure 14. Analysis of multipathing for three events in the observed data (top row) with synthetics from models M1 to M4 in the rows beneath (labeled on the right). For each event, the same frequency bands are used for the observed and synthetic data.

495 The 29 March 1998 event shows no multipathing in most of the models except for M4,
 496 but this has much weaker multipathing and both arrivals are different to their location
 497 in the observation. The strength of the velocity gradient of the boundary or its location
 498 in the tomography is not enough to reproduce the observation.

499 These varying results are to be expected with the inherent limitations of tomog-
 500 raphy described earlier. Due to the good agreement between synthetic data from model
 501 M3 and real observation for the 25 May 1997 event, we analyse the gradients sampled
 502 by this model. The gradients sampled by the mean 1D raypath for the event at 25 km
 503 depth intervals in model M3 is shown in Figure 15. The largest gradients sampled are
 504 not at the CMB but approximately 600 km above it, a similar depth to the maximum
 505 misfit found by Zhao et al. (2015) in their analysis of waveform broadening and the Pa-
 506 cific LLVP. The maximum gradient sampled is 0.7% δV_s per 100 km ($0.0005 \text{ km s}^{-1} \text{ km}^{-1}$)
 507 about 600 km above the CMB. This is an order of magnitude lower than found in some
 508 previous studies, which we discuss further in Section 5.2.

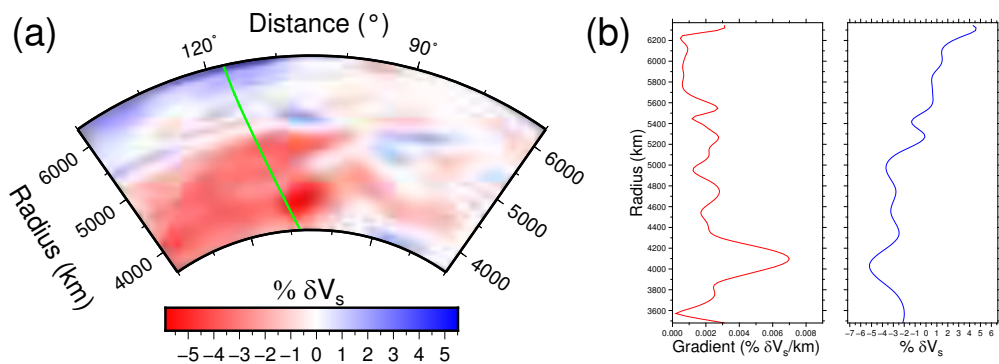


Figure 15. (a) Cross section of the receiver-side path of SKS from the 25 May 1997 event through M3. (b) two depth sections of the gradients and velocity perturbations sampled by the receiver-side 1-D path from event to average station location through model M3.

509 Although the modelled $\theta-p$ observation is similar, the modelled SKS data arrives
 510 much earlier than in the observations as shown in Figure 16. The difference in travel times
 511 is a reflection of the velocity perturbations sampled whereas the observation of multi-
 512 pathing is indicative of the gradients sampled. For this example, the gradient sampled
 513 over the raypath is sufficient to create similar multipathing as the observation, but the
 514 velocity perturbations are not sufficient to replicate the observed travel time residuals.

515 5.2 Comparison with previous studies

516 Many studies have analysed the African LLVP boundaries using travel time resid-
 517 uals and multipathing observations with forward modelling to infer properties such as
 518 the location, velocity gradient and inclination of the boundary (e.g. Ni et al., 2002; Sun
 519 & Miller, 2013; Sun et al., 2010; Ritsema et al., 1998; Wang & Wen, 2004). As there is
 520 extensive analysis of the structures in the regions we have analysed, we compare the find-
 521 ings of the relevant studies to our own.

522 From travel time residuals and waveform analysis, several studies have inferred the
 523 velocity gradients at the boundaries and perturbations inside the African LLVP (Ni et
 524 al., 2002; Sun & Miller, 2013; Wang & Wen, 2007b; Ritsema et al., 1998). We assume
 525 the gradient of the boundary is the main cause of the observed multipathing. As only
 526 one of our models matches well with the observation, we only compare the gradient we
 527 found to produce multipathing for the 25 May 1997 event with other studies (See Ta-

Event: 1997-05-25

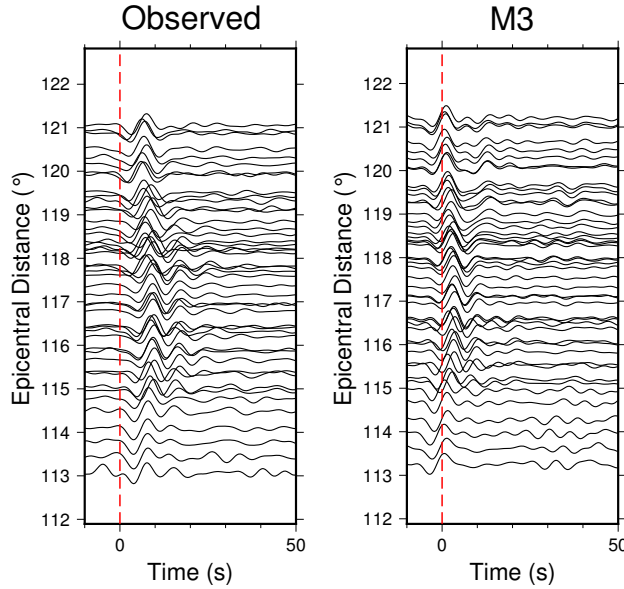


Figure 16. Record sections of the observed data (left) and the synthetic data from M3 (right) for the 25 May 1997 event. Despite producing multipathing in the $\theta-p$ plots, the travel time are much closer to the PREM (Dziewonski & Anderson, 1981) predicted SKS arrival time (dashed red line). The modeled waveforms arrive significantly earlier than the observations. We suggest the negative velocity perturbations in the model are not strong enough or the positive perturbations are too strong.

ble 1). Gradients up to 0.7% δV_s per 100 km ($0.00050 \text{ km s}^{-1} \text{ km}^{-1}$) are required to produce similar observations for the 25 May 1997 event which is an order of magnitude lower than the strongest estimated gradients of -3% δV_s per 50 km ($0.044 \text{ km s}^{-1} \text{ km}^{-1}$) (Ni et al., 2002), though similar to that found by Ritsema et al. (1998) -2% δV_s per 300 km ($0.00048 \text{ km s}^{-1} \text{ km}^{-1}$). We discuss possible reasons for this weaker gradient below.

Our observations analyse coherent signals across the array by stacking many waveforms together and not analysing them individually. Each measurement is sensitive to a larger region and could lead to boundary structures being sampled for longer, therefore weaker gradients are required to produce multipathing. Previous estimates of the stronger gradients used 2-D forward modelling to replicate their observations (Ni et al., 2002; Ni & Helmberger, 2003b). Any travel time delay or multipathing would have to be from in-plane structures and contributions from out of plane structure would not be accounted for. We use 3-D full wavefield modelling thus accounting for contributions from out of plane structures which could lead to a weaker gradient estimation. The effect of a wider region of influence from array methodology on a full wavefield sampling a 3-D anomaly structure could explain the difference between our gradient estimate and that of previous studies.

The presence of strong velocity gradients at LLVP boundaries causing multipathing and sharp changes in travel time residuals is commonly used as evidence for a thermochemical origin of LLVPs (Ni et al., 2002; To et al., 2005; Ritsema et al., 1998). We require gradients an order of magnitude lower than previous estimates to produce multipathing similar to our observations. The gradients of 0.7 % δV_s per 100 km ($0.00050 \text{ km s}^{-1} \text{ km}^{-1}$) are well below those evident in purely thermal models (2.25 % δV_s over 50

551 km ($0.0032 \text{ km s}^{-1} \text{ km}^{-1}$) (Schuberth et al., 2009) and $3.5 - 4.5\%$ δV_s per 100 km (0.0025
552 – $0.0032 \text{ km s}^{-1} \text{ km}^{-1}$) (Davies et al., 2012)). This modelling implies that velocity gra-
553 dients capable of producing observable multipathing cannot distinguish between ther-
554 mal and thermochemical LLVPs.

555 **6 Conclusions**

556 Through measuring the backazimuth and horizontal slowness of SKS and SKKS
 557 data sampling the lower mantle beneath Africa, we identify clear multipathing in approx-
 558 imately 16 % of our whole array observations and 8.0 % of our sub array observations.
 559 We find evidence for wavefield perturbation from backazimuth deviations of up to 22°
 560 and horizontal slowness deviations of up to 1.2 s/°. Spatial analysis of these measure-
 561 ments relative to structure resolved by seismic tomography gives evidence for a circu-
 562 lar feature to the southeast of Africa, adjacent fast and slow structures and an LLVP bound-
 563 ary. This suggests that tomography models, while limited, do resolve some structure that
 564 provide explanations for our observations.

565 We conduct full wavefield forward modelling to constrain what lateral velocity gra-
 566 dients are needed to reproduce our observations. We find gradients of up to 0.7 % δV_s
 567 per 100 km ($0.00050 \text{ km s}^{-1} \text{ km}^{-1}$) sampled approximately 600 km above the CMB are
 568 required to reproduce our multipathing observations. This is an order of magnitude lower
 569 than previous estimates of $-3\% \delta V_s$ per 50 km ($0.0044 \text{ km s}^{-1} \text{ km}^{-1}$) (Ni et al., 2002),
 570 which is commonly used to argue for a thermochemical origin of LLVPs. As the gradi-
 571 ents we predict are well below the largest estimates for both thermal and thermochem-
 572 ical structures (Davies et al., 2012), we argue multipathing observation caused by lat-
 573 eral velocity gradients of LLVP boundaries is not necessarily evidence for a thermochem-
 574 ical composition.

575 **Acknowledgments**

576 This research is supported by the NERC DTP Spheres grant NE/L002574/1. Predic-
 577 tions were made using the Taup toolkit (Crotwell et al., 1999). Figures made using GMT
 578 (Wessel et al., 2013). Data was retrieved from IRIS Data Center (<http://www.iris.edu>)
 579 using ObspyDMT (Hosseini & Sigloch, 2017), events used are provided in the supple-
 580 mentary material. There are no financial conflicts of interest for any authors.

581 **References**

- 582 Bijwaard, H., Spakman, W., & Engdahl, E. R. (1998). Closing the gap between
 583 regional and global travel time tomography. *Journal of Geophysical Research: Solid Earth*, *103*(B12), 30055–30078.
- 584 Blandford, R. R. (1974). An automatic event detector at the Tonto Forest seismic
 585 observatory. *Geophysics*, *39*(5), 633–643.
- 586 Bull, A. L., McNamara, A. K., Becker, T. W., & Ritsema, J. (2010). Global scale
 587 models of the mantle flow field predicted by synthetic tomography models.
 588 *Physics of the Earth and Planetary Interiors*, *182*(3-4), 129–138.
- 589 Bull, A. L., McNamara, A. K., & Ritsema, J. (2009). Synthetic tomography of
 590 plume clusters and thermochemical piles. *Earth and Planetary Science Letters*,
 591 *278*(3), 152–162.
- 592 Christensen, U. R., & Hofmann, A. W. (1994). Segregation of subducted oceanic
 593 crust in the convecting mantle. *Journal of Geophysical Research: Solid Earth*,
 594 *99*(B10), 19867–19884.
- 595 Cottaar, S., & Romanowicz, B. (2013). Observations of changing anisotropy across
 596 the southern margin of the African LLVP. *Geophysical Journal International*,
 597 *195*(2), 1184–1195.
- 598 Crotwell, H. P., Owens, T. J., & Ritsema, J. (1999). The TauP Toolkit: Flexi-
 599 ble seismic travel-time and ray-path utilities. *Seismological Research Letters*,
 600 *70*(2), 154–160.
- 601 Davaille, A. (1999). Simultaneous generation of hotspots and superswells by convec-
 602 tion in a heterogeneous planetary mantle. *Nature*, *402*(6763), 756–760.
- 603 Davies, D. R., Goes, S., Davies, J. H., Schuberth, B. S. A., Bunge, H.-P., & Ritsema,
 604

- 605 J. (2012). Reconciling dynamic and seismic models of Earth's lower mantle:
 606 The dominant role of thermal heterogeneity. *Earth and Planetary Science
 607 Letters*, *353*, 253–269.
- 608 Davies, D. R., Goes, S., & Lau, H. C. P. (2015). Thermally dominated deep man-
 609 ture LLSVPs: a review. In *The earth's heterogeneous mantle* (pp. 441–477).
 610 Springer.
- 611 Davies, D. R., Goes, S., & Sambridge, M. (2015). On the relationship between
 612 volcanic hotspot locations, the reconstructed eruption sites of large igneous
 613 provinces and deep mantle seismic structure. *Earth and Planetary Science
 614 Letters*, *411*, 121–130.
- 615 Deschamps, F., Cobden, L., & Tackley, P. J. (2012). The primitive nature of large
 616 low shear-wave velocity provinces. *Earth and Planetary Science Letters*, *349*,
 617 198–208.
- 618 Dziewonski, A. M., & Anderson, D. L. (1981). Preliminary reference Earth model.
 619 *Physics of the earth and planetary interiors*, *25*(4), 297–356.
- 620 Ford, H. A., Long, M. D., He, X., & Lynner, C. (2015). Lowermost mantle flow at
 621 the eastern edge of the African Large Low Shear Velocity Province. *Earth and
 622 Planetary Science Letters*, *420*, 12–22.
- 623 Foulger, G. R., Panza, G. F., Artemieva, I. M., Bastow, I. D., Cammarano, F.,
 624 Evans, J. R., ... Yanovskaya, T. B. (2013). Caveats on tomographic images.
 625 *Terra Nova*, *25*(4), 259–281.
- 626 French, S. W., & Romanowicz, B. A. (2014). Whole-mantle radially anisotropic
 627 shear velocity structure from spectral-element waveform tomography. *Geophys-
 628 ical Journal International*, *199*(3), 1303–1327.
- 629 Frost, D. A., & Rost, S. (2014). The P-wave boundary of the large-low shear ve-
 630 locity province beneath the Pacific. *Earth and Planetary Science Letters*, *403*,
 631 380–392.
- 632 Garnero, E. J., McNamara, A. K., & Shim, S.-H. (2016). Continent-sized anomalous
 633 zones with low seismic velocity at the base of Earth's mantle. *Nature Geo-
 634 science*, *9*(7), 481–489.
- 635 Grand, S. P. (2002). Mantle shear-wave tomography and the fate of subducted
 636 slabs. *Philosophical Transactions of the Royal Society of London A: Mathemat-
 637 ical, Physical and Engineering Sciences*, *360*(1800), 2475–2491.
- 638 Grand, S. P., van der Hilst, R. D., & Widjiantoro, S. (1997). High resolution global
 639 tomography: a snapshot of convection in the Earth. *Geological Society of
 640 America Today*, *7*(4).
- 641 Hager, B. H. (1984). Subducted slabs and the geoid: Constraints on mantle rheology
 642 and flow. *Journal of Geophysical Research: Solid Earth*, *89*(B7), 6003–6015.
- 643 Hager, B. H., Clayton, R. W., Richards, M. A., Comer, R. P., & Dziewonski, A. M.
 644 (1985). Lower mantle heterogeneity, dynamic topography and the geoid. *Na-
 645 ture*, *313*(6003), 541.
- 646 He, Y., & Wen, L. (2009). Structural features and shear-velocity structure of the
 647 “Pacific Anomaly”. *Journal of Geophysical Research: Solid Earth*, *114*(B2).
- 648 He, Y., & Wen, L. (2012). Geographic boundary of the “Pacific Anomaly” and its
 649 geometry and transitional structure in the north. *Journal of Geophysical Re-
 650 search: Solid Earth*, *117*(B9).
- 651 He, Y., Wen, L., & Zheng, T. (2006). Geographic boundary and shear wave velocity
 652 structure of the “Pacific anomaly” near the core–mantle boundary beneath
 653 western Pacific. *Earth and Planetary Science Letters*, *244*(1), 302–314.
- 654 Hirose, K., Fei, Y., Ma, Y., & Mao, H.-K. (1999). The fate of subducted basaltic
 655 crust in the Earth's lower mantle. *Nature*, *397*(6714), 53–56.
- 656 Hirose, K., Takafuji, N., Sata, N., & Ohishi, Y. (2005). Phase transition and den-
 657 sity of subducted MORB crust in the lower mantle. *Earth and Planetary Sci-
 658 ence Letters*, *237*(1-2), 239–251.

- 659 Hosseini, K., & Sigloch, K. (2017). obspyDMT: a Python toolbox for retrieving and
 660 processing of large seismological datasets. *Solid Earth*, 8.
- 661 Hutko, A. R., Bahavar, M., Trabant, C., Weekly, R. T., Fossen, M. V., & Ahern, T.
 662 (2017). Data products at the IRIS-DMC: Growth and usage. *Seismological
 663 Research Letters*, 88(3), 892–903.
- 664 Ishii, M., & Tromp, J. (1999). Normal-Mode and Free-Air Gravity Constraints
 665 on Lateral Variations in Velocity and Density of Earth's Mantle. *Science*,
 666 285(5431), 1231–1236.
- 667 James, D., Fouch, M., VanDecar, J., Van Der Lee, S., & Group, K. S. (2001). Tecto-
 668 spheric structure beneath southern Africa. *Geophysical research letters*, 28(13),
 669 2485–2488.
- 670 Koelemeijer, P., Deuss, A., & Ritsema, J. (2017). Density structure of Earth's low-
 671 ermost mantle from Stoneley mode splitting observations. *Nature Communications*, 8.
- 672 Koelemeijer, P., Ritsema, J., Deuss, A., & Van Heijst, H.-J. (2015). SP12RTS: a
 673 degree-12 model of shear-and compressional-wave velocity for Earth's mantle.
 674 *Geophysical Journal International*, 204(2), 1024–1039.
- 675 Komatitsch, D., & Tromp, J. (2002a). Spectral-element simulations of global seis-
 676 mic wave propagation-II. Three-dimensional models, oceans, rotation and
 677 self-gravitation. *Geophysical Journal International*, 150(1), 303–318.
- 678 Komatitsch, D., & Tromp, J. (2002b). Spectral-element simulations of global seismic
 679 wave propagation-I. Validation. *Geophysical Journal International*, 149(2),
 680 390–412.
- 681 Krischer, L., Hutko, A. R., Van Driel, M., Stähler, S., Bahavar, M., Trabant, C., &
 682 Nissen-Meyer, T. (2017). On-demand custom broadband synthetic seismo-
 683 grams. *Seismological Research Letters*, 88(4), 1127–1140.
- 684 Labrosse, S., Hernlund, J., & Coltice, N. (2007). A crystallizing dense magma ocean
 685 at the base of the Earth's mantle. *Nature*, 450(7171), 866–869.
- 686 Lau, H. C., Mitrovica, J. X., Davis, J. L., Tromp, J., Yang, H.-Y., & Al-Attar, D.
 687 (2017). Tidal tomography constrains Earth's deep-mantle buoyancy. *Nature*,
 688 551(7680), 321.
- 689 Lee, C.-T. A., Luffi, P., Höink, T., Li, J., Dasgupta, R., & Hernlund, J. (2010).
 690 Upside-down differentiation and generation of a 'primordial' lower mantle.
 691 *Nature*, 463(7283), 930–933.
- 692 Lekic, V., Cottaar, S., Dziewonski, A., & Romanowicz, B. (2012). Cluster analysis of
 693 global lower mantle tomography: A new class of structure and implications for
 694 chemical heterogeneity. *Earth and Planetary Science Letters*, 357, 68–77.
- 695 Li, M., & McNamara, A. K. (2013). The difficulty for subducted oceanic crust to
 696 accumulate at the Earth's core-mantle boundary. *Journal of Geophysical Re-
 697 search: Solid Earth*, 118(4), 1807–1816.
- 698 Lithgow-Bertelloni, C., & Silver, P. G. (1998). Dynamic topography, plate driving
 699 forces and the African superswell. *Nature*, 395(6699), 269.
- 700 Lucy, L. B. (1974). An iterative technique for the rectification of observed distribu-
 701 tions. *The Astronomical Journal*, 79, 745.
- 702 Lynner, C., & Long, M. D. (2014). Lowermost mantle anisotropy and deforma-
 703 tion along the boundary of the African LLSVP. *Geophysical Research Letters*,
 704 41(10), 3447–3454.
- 705 Masters, G., Laske, G., Bolton, H., & Dziewonski, A. (2000). The relative behavior
 706 of shear velocity, bulk sound speed, and compressional velocity in the mantle:
 707 implications for chemical and thermal structure. *Earth's deep interior: mineral
 708 physics and tomography from the atomic to the global scale*, 63–87.
- 709 Maupin, V. (2011). Upper-mantle structure in southern Norway from beamform-
 710 ing of Rayleigh wave data presenting multipathing. *Geophysical Journal Inter-
 711 national*, 185(2), 985–1002.
- 712 McNamara, A. K., Garnero, E. J., & Rost, S. (2010). Tracking deep mantle reser-

- 714 voirs with ultra-low velocity zones. *Earth and Planetary Science Letters*,
 715 299(1), 1–9.
- 716 McNamara, A. K., & Zhong, S. (2004). Thermochemical structures within a spherical
 717 mantle: Superplumes or piles? *Journal of Geophysical Research: Solid*
 718 *Earth*, 109(B7).
- 719 McNamara, A. K., & Zhong, S. (2005). Thermochemical structures beneath Africa
 720 and the Pacific Ocean. *Nature*, 437(7062), 1136–1139.
- 721 Mound, J., Davies, C., Rost, S., & Aurnou, J. (2019). Regional stratification at the
 722 top of Earth's core due to core–mantle boundary heat flux variations. *Nature*
 723 *Geoscience*, 12(7), 575–580.
- 724 Mulyukova, E., Steinberger, B., Dabrowski, M., & Sobolev, S. V. (2015). Survival of
 725 LLSVPs for billions of years in a vigorously convecting mantle: replenishment
 726 and destruction of chemical anomaly. *Journal of Geophysical Research: Solid*
 727 *Earth*, 120(5), 3824–3847.
- 728 Ni, S., & Helmberger, D. V. (2003a). Further constraints on the African superplume
 729 structure. *Physics of the Earth and Planetary Interiors*, 140(1-3), 243–251.
- 730 Ni, S., & Helmberger, D. V. (2003b). Ridge-like lower mantle structure beneath
 731 south Africa. *Journal of Geophysical Research: Solid Earth*, 108(B2).
- 732 Ni, S., & Helmberger, D. V. (2003c). Seismological constraints on the South African
 733 superplume; could be the oldest distinct structure on Earth. *Earth and Plane-*
 734 *tary Science Letters*, 206(1-2), 119–131.
- 735 Ni, S., Tan, E., Gurnis, M., & Helmberger, D. (2002). Sharp sides to the African su-
 736 perplume. *Science*, 296(5574), 1850–1852.
- 737 Picozzi, M., Parolai, S., & Bindi, D. (2010). Deblurring of frequency–wavenumber
 738 images from small-scale seismic arrays. *Geophysical Journal International*,
 739 181(1), 357–368.
- 740 Reiss, M., Long, M., & Creasy, N. (2019). Lowermost Mantle Anisotropy Beneath
 741 Africa From Differential SKS-SKKS Shear-Wave Splitting. *Journal of Geophys-*
 742 *ical Research: Solid Earth*.
- 743 Richardson, W. H. (1972). Bayesian-based iterative method of image restoration.
 744 *JOSA*, 62(1), 55–59.
- 745 Ritsema, J., Deuss, A. A., Van Heijst, H. J., & Woodhouse, J. H. (2011). S40RTS: a
 746 degree-40 shear-velocity model for the mantle from new Rayleigh wave disper-
 747 sion, teleseismic traveltimes and normal-mode splitting function measurements.
 748 *Geophysical Journal International*, 184(3), 1223–1236.
- 749 Ritsema, J., McNamara, A. K., & Bull, A. L. (2007). Tomographic filtering of geo-
 750 dynamic models: Implications for model interpretation and large-scale mantle
 751 structure. *Journal of Geophysical Research: Solid Earth*, 112(B1).
- 752 Ritsema, J., Ni, S., Helmberger, D. V., & Crotwell, H. P. (1998). Evidence for strong
 753 shear velocity reductions and velocity gradients in the lower mantle beneath
 754 Africa. *Geophysical Research Letters*, 25(23), 4245–4248.
- 755 Rost, S., & Thomas, C. (2002). Array seismology: Methods and applications. *Re-*
 756 *views of geophysics*, 40(3).
- 757 Roy, S. K., Takeuchi, N., Srinagesh, D., Ravi Kumar, M., & Kawakatsu, H. (2019).
 758 Topography of the western Pacific LLSVP constrained by S-wave multipathing.
 759 *Geophysical Journal International*, 218(1), 190–199.
- 760 Schimmel, M., & Paulssen, H. (1997). Noise reduction and detection of weak, coher-
 761 ent signals through phase-weighted stacks. *Geophysical Journal International*,
 762 130(2), 497–505.
- 763 Schubert, G., Masters, G., Olson, P., & Tackley, P. (2004). Superplumes or plume
 764 clusters? *Physics of the Earth and Planetary Interiors*, 146(1), 147–162.
- 765 Schuberth, B. S. A., Bunge, H.-P., & Ritsema, J. (2009). Tomographic filtering
 766 of high-resolution mantle circulation models: Can seismic heterogeneity be
 767 explained by temperature alone? *Geochemistry, Geophysics, Geosystems*,
 768 10(5).

- 769 Silver, P. G., & Chan, W. W. (1986). Observations of body wave multipathing from
 770 broadband seismograms: evidence for lower mantle slab penetration beneath
 771 the Sea of Okhotsk. *Journal of Geophysical Research: Solid Earth*, 91(B14),
 772 13787–13802.
- 773 Simmons, N. A., Forte, A. M., Boschi, L., & Grand, S. P. (2010). GyPSuM: A joint
 774 tomographic model of mantle density and seismic wave speeds. *Journal of Geo-*
 775 *physical Research: Solid Earth*, 115(B12).
- 776 Su, W.-j., & Dziewonski, A. M. (1997). Simultaneous inversion for 3-D variations in
 777 shear and bulk velocity in the mantle. *Physics of the Earth and Planetary In-*
 778 *teriori*, 100(1-4), 135–156.
- 779 Sun, D., Gurnis, M., Saleeby, J., & Helmberger, D. (2017). A dipping, thick segment
 780 of the Farallon Slab beneath central US. *Journal of Geophysical Research: Solid*
 781 *Earth*, 122(4), 2911–2928.
- 782 Sun, D., Helmberger, D., & Gurnis, M. (2010). A narrow, mid-mantle plume below
 783 southern Africa. *Geophysical Research Letters*, 37(9).
- 784 Sun, D., Helmberger, D., Lai, V. H., Gurnis, M., Jackson, J. M., & Yang, H.-Y.
 785 (2019). Slab Control on the Northeastern Edge of the Mid-Pacific LLSVP near
 786 Hawaii. *Geophysical Research Letters*.
- 787 Sun, D., Helmberger, D., Ni, S., & Bower, D. (2009). Direct measures of lateral
 788 velocity variation in the deep Earth. *Journal of Geophysical Research: Solid*
 789 *Earth*, 114(B5).
- 790 Sun, D., & Miller, M. S. (2013). Study of the western edge of the African large low
 791 shear velocity province. *Geochemistry, Geophysics, Geosystems*, 14(8), 3109–
 792 3125.
- 793 Tackley, P. J. (1998). Three-Dimensional Simulations of Mantle Convection with
 794 a Thermo-Chemical Basal Boundary Layer: D''? *The core-mantle boundary re-*
 795 *gion*, 231–253.
- 796 Tackley, P. J. (2011). Living dead slabs in 3-D: The dynamics of compositionally-
 797 stratified slabs entering a “slab graveyard” above the core-mantle boundary.
Physics of the Earth and Planetary Interiors, 188(3-4), 150–162.
- 798 Thorne, M. S., Garnero, E. J., & Grand, S. P. (2004). Geographic correlation be-
 800 tween hot spots and deep mantle lateral shear-wave velocity gradients. *Physics*
 801 *of the Earth and Planetary Interiors*, 146(1), 47–63.
- 802 To, A., Romanowicz, B., Capdeville, Y., & Takeuchi, N. (2005). 3D effects of sharp
 803 boundaries at the borders of the African and Pacific Superplumes: Observation
 804 and modeling. *Earth and Planetary Science Letters*, 233(1), 137–153.
- 805 Tolstikhin, I., & Hofmann, A. W. (2005). Early crust on top of the earth’s core.
Physics of the Earth and Planetary Interiors, 148(2-4), 109–130.
- 806 Torsvik, T. H., Burke, K., Steinberger, B., Webb, S. J., & Ashwal, L. D. (2010).
 807 Diamonds sampled by plumes from the core-mantle boundary. *Nature*,
 808 466(7304), 352–355.
- 809 Wang, Y., & Wen, L. (2004). Mapping the geometry and geographic distribution of
 810 a very low velocity province at the base of the Earth’s mantle. *Journal of Geo-*
 811 *physical Research: Solid Earth*, 109(B10).
- 812 Wang, Y., & Wen, L. (2007a). Complex seismic anisotropy at the border of a very
 813 low velocity province at the base of the Earth’s mantle. *Journal of Geophysical*
 814 *Research: Solid Earth*, 112(B9).
- 815 Wang, Y., & Wen, L. (2007b). Geometry and P and S velocity structure of the
 816 “African Anomaly”. *Journal of Geophysical Research: Solid Earth*, 112(B5).
- 817 Wen, L., Silver, P., James, D., & Kuehnel, R. (2001). Seismic evidence for a thermo-
 818 chemical boundary at the base of the Earth’s mantle. *Earth and Planetary Sci-*
 819 *ence Letters*, 189(3), 141–153.
- 820 Wessel, P., Smith, W. H., Scharroo, R., Luis, J., & Wobbe, F. (2013). Generic map-
 821 ping tools: improved version released. *Eos, Transactions American Geophysical*
 822 *Union*, 94(45), 409–410.

- 824 Zhao, C., Garnero, E. J., McNamara, A. K., Schmerr, N., & Carlson, R. W. (2015).
825 Seismic evidence for a chemically distinct thermochemical reservoir in Earth's
826 deep mantle beneath Hawaii. *Earth and Planetary Science Letters*, 426, 143–
827 153.